Politecnico di Milano

Scuola di Ingegneria Industriale e dell'Informazione

Corso di Laurea Magistrale in Engineering Physics

Electrical and optical characterization of spin polarized electron diffusion in graphene/Ge heterostructures

Supervisor:

Dr. Federico Bottegoni

Candidate:

Tommaso Marelli

Matr. 915798

Academic Year 2020/2021

Abstract

Since its discovery in 2004, graphene turned out to be a novel material in many electronics applications, where it can be used as a 2D transparent electrode with very high mobility and large current capability. Among its applications, recent works have investigated the possibility of using graphene also in spintronics , where, thanks to the low spin-orbit interaction, it can be used as a spin transport channel with a large spin diffusion length (several micrometres at room temperature). In this thesis work, I have investigated the injection and transport of spin current in graphene, coupled to a low *n*-doped Ge substrate, forming a graphene/Ge Schottky junction. The spin current is generated in Ge by means of illumination with circularly polarized light, exploiting the phenomenon of optical orientation: thanks to the optical selection rules for direct transitions in semiconductors, the angular momentum of the photon is coupled to the spin degree of freedom of the photoexcited carriers. The electrons promoted in the conduction band of Ge present a net spin polarization and generate a spin current. The latter eventually diffuses from Ge to graphene and then in graphene itself, and finally reaching a thin Pt pad, where it can be detected thanks to inverse spin-Hall effect. The sample used for the experiments presented in this thesis has been fabricated at the L-Ness laboratories in Como, using electron beam lithography and a wet transfer technique for the transfer of graphene. The quality of the graphene/Ge Schottky junction has been tested by means of an electrical characterization, which has shown the correct rectifying behaviour as predicted from the thermionic emission theory.

From the characterization of the ISHE signal, The transfer of a spin current from a semiconductor (Ge) and graphene through a Schottky contact has been demonstrated as well as the transport of spin polarized carriers in graphene has been achieved.

Sommario

Sin dalla sua scoperta nel 2004, il grafene si è dimostrato essere un materiale rivoluzionario in molte applicazioni elettroniche, dove viene usato come elettrodo 2D trasparente con un'elevata mobilità dei portatori. Tra le sue molte applicazioni, recenti studi hanno evidenziato la possibilità di utilizzare il grafene nella spintronica, dove, grazie alla piccola interazione di spin orbita, può essere utilizzato come canale per il transporto di spin con un'elevata lunghezza di diffusione dello spin. In questo lavoro, ho studiato l'iniezione e il trasporto di spin nel grafene, accoppiandolo con un substrato di Ge leggermente drogato *n*, a formare una giunzione Schottky grafene/Ge. La corrente di spin viene generata nel Ge illuminandolo con luce polarizzata circolarmente. Grazie alle regole di selezione per transizioni ottiche di dipoli elettrico nei semiconduttori, il momento angolare dei fotoni viene accoppiato con lo spin dei portatori fotoeccitati. In questo modo, gli elettroni promossi nella banda di conduzione del Ge presentano una polarizzazione di spin netta e, diffondendo, generano una corrente di spin. Quest'ultima può a questo punto diffondere nel grafene. In tal caso, la corrente di spin raggiunge un sottile film di Pt dove, tramite effetto spin-Hall inverso, genera una differenza di potenziale ai capi del Pt. Misurando questa differenza di potenziale, siamo in grado di determinare se l'iniezione e il trasporto di spin nel grafene ha avuto successo. Il campione utilizzato per gli esperimenti è stato fabbricato presso i laboratori L-Ness di Como, usando litografia elettronica, mentre il grafene è stato traferito sulla struttura usando una tecnica di *wet transfer*. La qualità della giunzione Schottky grafene/Ge è stata testata facendo una caratterizzazione elettrica, che ha mostrato il corretto andamento rettificante, come predetto dalla teoria di emissione termoionica. Dalla caratterizzazione del segnale ISHE è stata sperimentalmente dimostrato il trasferimento di una corrente di spin da un semiconduttore (Ge) al grafene attravero una giunzione Schottky grafene/Ge, così come il trasporto all'interno del grafene medesimo fino al film di Pt è stato ottenuto.

Contents

List of Figures vii

List of Tables xi

Introduction 1

1. Graphene/semiconductor Schottky junction 3

1.1. Metal/semiconductor Schottky junction. 3

1.2. Graphene/semiconductor Schottky junction. 6

1.3. Light-graphene/SC interaction. 10

2. Photoinduced inverse spin-Hall effect 12

2.1. Spin optical orientation in direct gap semiconductors. 12

2.1.1. Conduction and valence band in direct gap semiconductors. 13

2.1.2. Interaction with circularly polarized light. 19

2.1.3. Optical orientation in Ge. 21

2.2. Inverse spin-Hall detection. 23

3. Graphene/Ge sample: design and fabrication 29

3.1. Sample design. 29

3.2. Sample fabrication. 31

3.2.1. Graphene wet transfer. 32

3.2.2. Graphene etching. 34

3.2.3. Pt detector and Ti/Au contacts deposition. 37

4. Eletro-optical characterization 42

4.1. I-V characterization. 42

4.2. Temperature dependent I-V characterization. 49

4.3. Optical characterization. 54

5. ISHE measurement 56

5.1. Setup for generation and measurement of spin-to-charge conversion. . . .56

5.1.1. Laser source. 58

5.1.2. Generation of modulated CPL. 59
5.1.3. Illumination at grazing incidence. 62
5.1.4. Lock-in measurement of ΔV. 63
5.2. Characterization of the ISHE signal. 64
5.2.1. Photon energy dependence of the ISHE signal. 64
5.2.2. ISHE as a function of the degree of circular polarization and light power. 66
5.2.3. Measurement of the signal phase. 68
5.2.4. Analysis of the ISHE signal for different position of the spot. 69

Conclusions **71**

Bibliography **73**

List of Figures

1.1 Barrier formation in metal/semiconductor junction according to Schottky model. The upper and the lower part show the band diagrams before and after contact, respectively. If $\varphi_M < \varphi_S$, the bands in SC are bended downward forming the accumulation contact type (**a**). If $\varphi_M = \varphi_S$ (**b**), the bands remain flat making a neutral contact. If $\varphi_M > \varphi_S$, SC bands bend upward making a depletion contact. Figure adapted from Ref. [5]. 4

1.2 Emission mechanisms for different doping level in n-doped semiconductor. As Nd increases, the depletion layer gets narrower and tunnelling is enhanced. Figure adapted from Ref.[5]. 6

1.3 (**a**) First Brillouin zone in reciprocal space. $\mathbf{b}_1$ and $\mathbf{b}_2$ are the generators of the reciprocal lattice. The six corners of the hexagonal Brillouin zone are the Dirac points, K and K' are the two non-equivalent points. Figure adapted from Ref. [24]. (**b**) conduction (top) and valence (down) band in the first Brillouin zone. It can be seen that the two bands are symmetric. (**c**) Dirac cones at the K point. Figure adapted from Ref. [4]. 7

1.4 Fermi level shift and associated φ_B shift in graphene/SC junction. (**a**) zero bias; (**b**) forward bias: φ_B increases; (**c**) reverse bias, φ_B decreases. Figure adapted from Ref. [22]. 9

1.5 Band diagrams of graphene/SC junction in case of (**a**) darkness under zero bias; (**b**) illumination under forward bias; (**c**) illumination under reverse bias. Figure adapted from Ref.[4]. 10

1.6 I-V curve for a graphene/n-Si junction for different incident power. The dashed line represents the ideal photodiode behaviour at P=1.65mW. It is evident the photocurrent drop as bias approaches the forward regime. Figure adapted from Ref. [23]. 11

2.1 1D chain of atoms separated by a distance a. The origin is placed on the atomic site indicated by the red dot. The black curve shows the behaviour of the periodic crystal potential, the red curve is the atomic potential of the atom centred centred in the origin and the green curve is the perturbation term $\Delta U(r)$. 14

2.2 Schematic rapresentation of overlap integral in case of **(a)** s-type orbitlas and **(b)** p-type orbitals. Figure adapted from Ref. [37]. 15

2.3 Conduction and valence band for a direct gap semiconductor (GaAs) in the presence of a relevant spin-orbit coupling. Figure adapted from Ref [19]. 16

2.4 States involved in the direct transition at Γ point and relative strength. Red (blue) arrows show transitions induced by right(left)-circularly polarized light. Values of angular momentum are expressed in unit of ħ. Figure adapted from [37]. 22

2.5 **(a)** Band structure of Ge. Figure adapted from Ref. [36]. **(b)** Degree of spin polarization (DSP) for electrons -black line- and holes -red dashed line- optically injected in Ge by means of LCP light as function of the photon energy. Figure adapted from Ref. [26]. 23

2.6 Spin-Hall effect. An unpolarized current in the x-direction generates a pure spin current on the y-direction and a spin-Hall voltage. **(b)** Inverse spin-Hall effect. A spin current density J_s in the x-direction generates a charge current density J_c in the y direction and a voltage drop at the edges of the slab. 24

2.7 Schematic representation of Ge/Pt heterostructure used for photoinduced ISHE. 26

3.1 Top view **(a)** and vertical section **(b)** of the detector layout. 30

3.2 **(a)** Positions of different types of structures in the 7x7 matrix and **(b)** corresponding values of Pt-Ge distance. 31

3.3 Standard structure **(a)** and test structure **(b)** after the etching of the SiO_2 layer. 32

3.4 Main steps of graphene wet transfer: **(a)** graphene is CVD grown on top and bottom of a Cu foil. **(b)** PMMA is spin coated on top of the foil and back graphene is removed with oxygen plasma etching. **(c)** Cu is etched in acid solution while PMMA gives the support for graphene. **(d)** The PMMA/graphene stack is rinsed in deionized water. **(d)** Fishing with the sample. 33

3.5 RIE chamber scheme. The sample is placed on the bottom plate, which is coupled by a capacitance to a RF source. Due to the positive potential of plasma and the negative potential on the bottom plate, ions are accelerated toward the bottom plate, where they react with the sample. Figure adapted from [39]. 35

3.6 Structures 1.2 **(a),** 2.5 **(b)** and the test structure 2.1 **(c)**. 36

3.7 Optical images taken in dark field mode of the structures after the graphene etching process is terminated. In dark filed microscopy, only the light scattered by the sample is focus on the detector. Dark field microscopy allows to image also transparent objects. **(a)** Structure 1.1. **(b)** Structure 7.3. 36

3.8 Lift off process with a PMMA bi-layer. **(a)** A high wight PMMA is spin-coated on top of a low weight PMMA and exposed to the electron beam. **(b)** PMMA is developed in a mixture of MIBK and IPA and the exposed layers of PMMA are removed, forming an enhanced undercut. **(c)** Metal deposition. **(d)** Thanks to the presence of the undercuts, acetone removes the remain PMMA with the metal on top. The metal remain only in the regions that were exposed. 38

3.9 Test structure 2.1 after the resist development, before the Pt deposition. 39

3.10 **(a)** Structure 1.2 after resist development, before Pt deposition. **(b)** Structure 1.2 after Pt deposition and lift-off. 39

3.11 Optical images of the final test **(a)** and standard structures **(b)**. 41

4.1 **(a)** Scheme of the electrical connection for the I-V characteristic measurement. **(b)** Picture of the probe used to connect the Au pad. 43

4.2 Forward and reverse bias current-voltage characteristic in linear (a) and semi-logarithmic (b) scale. 44

4.3 Equivalent circuit for the graphene/Ge Schottky diode, taking into account the series resistance. Figure adapted from [5]. 45

4.4 Linear fit performed to extrapolate the series resistance from the I-V characteristic for the structure 1.1. The linear fitting is performed between 0.9V and 1V. 46

4.5 **(a)** Semilogarithmic plot of current vs the effective voltage V_{eff} that drops on the junction, for the structure 1.1. The inset **(b)** shows the same characteristic in linear scale. 46

4.6 Linear fit of ln(I) vs V_{eff} for the structure 1.1. 47

4.7 Boxplot diagrams for the barrier height φ_b and n parameters of the 46 graphene/Ge Schottky structures. 49

4.8 Semilogarithmic current-voltage (I-V) characteristic of the graphene/Ge SBD in the temperature range 19°C-110°C in the forward and reverse bias range. 50

4.9 Semilogarithmic current-effective voltage (I-Veff) characteristic of the graphene/Ge SBD in the temperature range 19 °C-110 °C in the forward bias range. 50

4.10 Plot of φ_{ap} as a function of $1/2kT$. 51

4.11 Richardson plot of $\ln(Is/T^2)$ vs 1000/T for the graphene/Ge Schottky structure 3.2. 52

4.12 Modified Richardson plot obtained considering the barrier inhomogeneity effect, for the graphene/Ge structure 3.2. 53

4.13 Optical set-up for the I-V measurement under illumination. 54

4.14 I-V curve for the graphene/Ge photodiode under illumination at 0.8 eV for different intensities. As expected from a graphene/Ge photodiode, the photocurrent drops to zero at 0 bias. 55

5.1 Sketch of the optical generation and detection of spin currents in graphene. . .57

5.2 Experimental setup for the generation of spin current in graphene and measurement of the ISHE signal. 58

5.3 (**a**) Pellin-Broca prism used to separate the spectral components of the white light beam. By rotating the prism around the point O, we change the spectral component that is deviadet by 90°. (**b**) Power spectrum between 0.7eV-2 eV collected at the output of the fiber. 59

5.4 Degree of circularly polarization as function of time at the output of the PEM section, for different values of $\Delta\varphi_0$. The light entering the PEM is linearly polarized with an angle of 45° with respect to the PEM optical axis. 61

5.5 Spectral dynamics of the normalized ISHE signal for the structure 1.4, measured with a double modulation technique. 65

5.6 ISHE signal as a function of (**a**) the degree of circular polarization and (**b**) light beam power, for fixed photon energy of 0.8 eV. 67

5.7 Phase of the ISHE signal vs the rotation of the displacer. 68

5.8 Normalized ISHE signal for photon energy of 0.8eV as function of the distance between the centre of the spot and the Pt detector. 70

List of Tables

2.1 Clebsh-Gordan integrals for CB and VB states at Γ. Ref. [30]. 18

4.1 Experimental values of the Schottky barrier height for the graphene/Ge junctions, obtained from linear interpolation of ln (I) vs V_{eff}. Values are reported in eV. 48

4.2 Experimental values of the ideality index n for the graphene/Ge junctions, obtained from linear interpolation of ln(I) vs V_{eff}. 48

4.3 Experimental values for Schottky barrier and n as function of temperature. Values calculated by linear fitting ln(I) vs Veff. 49

4.4 Experimental values for $\overline{\varphi_b}$, σ and A^* obtained for the tested structures. Richardson constant is calculated using the modified Richardson plot. 53

Introduction

The aim of spintronics is to use the spin degree of freedom of carriers in order to manipulate and transport information [1]. In particular, the possibility of creating a pure spin current, i.e., a net spin flow with no net charge transport associated, allows for the implementation of low power dissipation devices [2]. One of the main tasks of spintronics is to develop suitable spin transport channel, with long spin lifetime and long spin diffusion length. In most cases, spin relaxation processes are caused by fluctuating effective magnetic fields generated by spin-orbit effect [18]. Spins start to precess around these magnetic fields and lose their coherence. In this regard, graphene seems to be a suitable material also for spintronics application. Indeed, thanks to the low atomic number of carbon, spin-orbit effect will be small in graphene ($H_{SO} \propto Z^4$) and therefore a long spin diffusion length is expected [1,3].

The most important issue of graphene in spintronics applications is that graphene is a non- magnetic material, therefore spin currents need to be somehow injected into it. Spin injection in graphene has been widely studied over the past years and includes spin injection from a ferromagnetic contact, optical injection, magnetism induced by means of defect or adatom engineering and magnetism induced by means of exploiting spin-orbit coupling [1-3]. In this thesis work, we tried to inject spin in graphene by couple it with a semiconductor, forming a graphene/semiconductor Schottky junction. Spin can be optically generated in the semiconductor by means of illumination with circularly polarized light. Thanks to optical selection rules, the spin momentum of the photons couple with the spin of the carriers and the photogenerated carriers present a net spin polarization [25]. Once the spin current is injected into graphene, it diffuses to a thin Pt layer where it is detected by means of inverse spin-Hall effect (ISHE). As a semiconductor, we used low n-doped ($N_D \approx 10^{16}$ cm^{-3}) Ge. Indeed, Ge has a direct bandgap of 0.8eV which is only 130meV bigger than the indirect gap and presents a large spin-orbit splitting (0.3eV) between the HH and LH bands and the SO bands at Γ. These features make Ge a perfect candidate for photogeneration of spin polarized electrons population, where polarization up to 50% can be reached [10,11,12,13]. Moreover, the 0.8eV direct bandgap of semiconductor perfectly matches the 1550 nm telecom wavelength making it a perfect candidate for spintronic-photonics

integration (e.g., conversion of light polarization information into electric voltage, by means of ISHE conversion of spin into an electromotive force [9]).

The thesis is thereby structured as follows: the first chapter presents the background theory of graphene/semiconductor Schottky junction, with a particular focus on how graphene modifies the standard metal/semiconductor junction. The second chapter introduces the main features of spin generation in Ge by means of illumination with circularly polarized light and its detection by means of ISHE. The third chapter illustrates the fabrication process of the device. The fourth chapter discusses and presents the results of the electrical characterization of the Gr/Ge Schottky junctions, in order to check the quality of the Schottky barrier and to determine its main parameters. Both the fabrication process and the electrical characterization were performed at the L-NESS laboratories in Como, in collaboration with the Nanoscale Device Group. The fifth chapter reports on the ISHE measurements for the device, performed at the SemiSpin LAB of the Physics Department of Politecnico di Milano.

Finally, conclusions are discussed together with possible future steps.

Chapter 1
Graphene/semiconductor Schottky junction

Thanks to its semi-metal nature, graphene can be used as a metal contact in Schottky junction with semiconductor (SC). At a first approximation, graphene/SC Schottky junctions behave as a standard Schottky junction, although, due to the finite density of states at the Dirac point, Fermi level in graphene is very sensitive to the injected carriers (electron or holes), making the Schottky barrier height (SBH) bias-dependent. This feature allows fabricating junctions with tuneable SBH [4,6].

In the following section, a review of standard Schottky junctions with lightly n-doped semiconductors is given and the most important features of thermionic emission in these systems is recalled. The model for thermionic emission in Schottky junctions is then adapted in the case of graphene/SC contacts.

1.1 Metal/semiconductor Schottky junction

When a metal and a semiconductor are put in contact, they can form an ohmic contact or a Schottky contact. The former is characterized by a linear current-voltage (I-V) behaviour, while the latter by a typical diode rectifying behaviour. The formation of the Schottky junction can be easily described by the Schottky-Mott theory, under the hypothesis that an intimate contact with no interfacial layer is formed. Let us assume that the semiconductor is n-doped: if the Fermi level of the metal $E_{F,M}$ is higher than the Fermi level of the semiconductor $E_{F,S}$,(both defined with respect to the free electrons energy level E_o), than the average energy of electrons is larger than in SC. Therefore, thermal equilibrium is established by a net

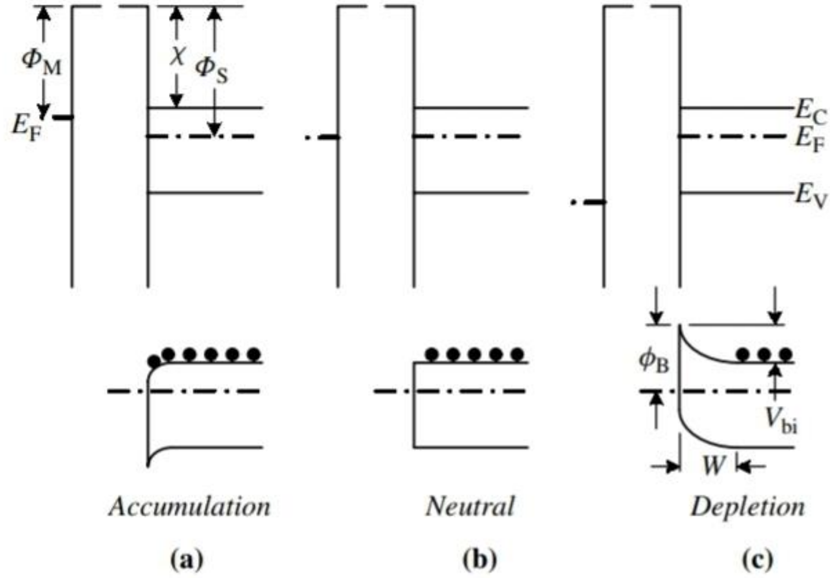

Fig 1.1 *Barrier formation in metal/semiconductor junction according to Schottky model. The upper and the lower part show the band diagrams before and after contact, respectively. If $\varphi_M < \varphi_S$, the bands in SC are bended downward forming the accumulation contact type **(a)**. If $\varphi_M = \varphi_S$ **(b)**, the bands remain flat making a neutral contact. If $\varphi_M > \varphi_S$, SC bands bend upward making a depletion contact. Figure adapted from Ref. [5].*

flow of electrons from the metal to the semiconductor, until the Fermi levels are aligned. The injected electrons are accumulated at the SC/metal interface, bending the conduction and valence band of SC downward (Fig 1.1 (a)). An ohmic contact is formed.

Schottky junction instead is formed when $E_{F,M} < E_{F,S}$. In this case, to reach thermal equilibrium, electrons flow from SC to the metal, leaving a positive space charged region, referred to as the depletion region w, with density given by the doping level N_D. The charge density generates a voltage drop which bends the SC bands upward, creating a barrier, the *built-in* potential (φ_{bi}), for electrons going from the semiconductor to the metal. As shown in Fig. 1.1, there is a discontinuity in the minimum available energy level at the interface, which forms a barrier blocking electrons from the metal to the SC, called the *Schottky barrier*. The value of the SBH is given by the Schottky-Mott rule [4,5]:

$$\varphi_B = \varphi_M - \chi, \tag{1.1.1}$$

where χ is the semiconductor electron affinity and φ_M is the metal work function. According to this simple relation, the SBH is just a function of the type of material

used to form the junction, it does not depend on doping concentration, and it is not changed by an applied bias, at variance with φ_{bi}. This is due to the high density of states in the metal, where a huge number of carriers can be injected just by slightly moving the Fermi level. The relation between the change of the electron density in the metal δn, induced by an applied voltage, and the associated Fermi level shift $\delta E_{F,m}$ is [4]:

$$\frac{\delta n}{n} = \frac{3}{2}\frac{\delta E_{F,m}}{E_{F,m}}. \qquad (1.1.2)$$

To preserve charge neutrality, δn need to be balanced by an equal change of carrier density in the semiconductor, which is limited by the doping density N_D. The equilibrium density n in the metal is typically of the order of $10^{22\div23}$ cm^{-3}, which is order of magnitudes larger than N_D ($10^{16\div19}$ cm^{-3}), thus giving a negligible change of the Fermi level in the metal.

Despite, according to the Schottky-Mott equation, φ_B only depends on φ_M and χ, Schottky-Tamm surface states in the gap of the semiconductor affect the barrier formation and, for high surface density of states, they pin the Fermi level at some point in the gap, making the barrier independent from the metal work function. Moreover, due to the many dangling bonds at the semiconductor surface, there is always a thin oxide layer at the interface providing for a voltage drop which makes φ_B slightly voltage dependent [4,5].

Even if the Schottky barrier is not dependent from the doping density, N_D is anyway an important parameter in determining the I-V characteristic of the junction. Indeed, N_D affects the extension of the depletion region, which is [4]:

$$w = \sqrt{\frac{2\varepsilon_s}{q^2 N_D}(\varphi_{bi} - qV - k_B T)}, \qquad (1.1.3)$$

where V is the applied bias, measured as the difference between the applied voltage on the metal side of the junction and the one applied on the semiconductor side. Therefore, V is positive in forward bias and negative in reverse bias. Using the dielectric constant for Ge $\varepsilon_{r,s} = 16.2$ and assuming for the term in parenthesis an order of 10^{-1} eV ($\varphi_{bi}{\sim}0.5\,eV$ and an applied forward bias of the same order, neglecting the small $k_B T$ term), Eq. (1.1.3) gives for Ge $w{\sim}1.33 \times 10^{10} nm/\sqrt{N_D(cm^{-3})}$.

When N_D is high ($N_D \gtrsim 10^{20} cm^{-3}$) [4,5], the barrier is narrowed ($w \lesssim 1$ nm for Ge) and electrons can tunnel through it diffusing into the metal; this is called field emission (FE) regime (fig.1.2 (c)). In case of light doping ($N_D \lesssim 3 \times 10^{17} cm^{-3}$),

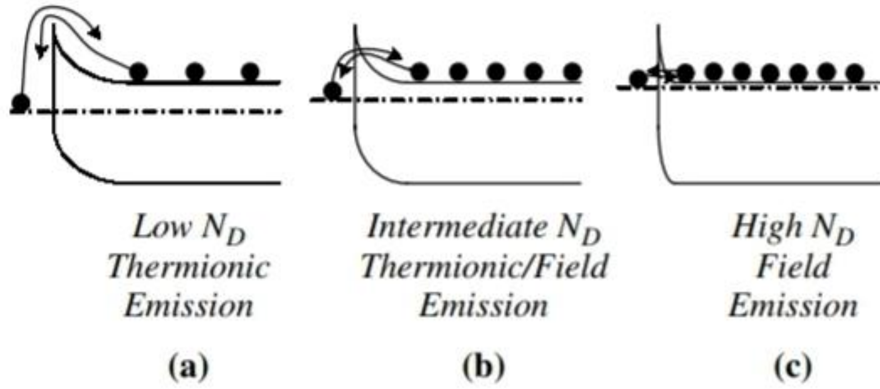

***Fig 1.2** Emission mechanisms for different doping level in n-doped semiconductor. As Nd increases, the depletion layer gets narrower and tunnelling is enhanced. Figure adapted from Ref.[5].*

the barrier is not sufficiently narrow ($w \gtrsim 25nm$ for Ge) to let electrons tunnelling and only the electrons thermally excited over the barrier can diffuse into the metal. When forward bias is applied, the barrier for the electrons from the semiconductor to the metal is reduced and the number of electrons injected into the metal exponentially increases. This is the so called thermionic emission (TE) regime (fig. 1.2 (a)). For intermediate doping levels, some electrons are thermally excited enough to tunnel through the barrier and this regime is called thermionic-field emission (TFE). For $N_D \sim 10^{16} cm^{-3}$,which is the doping level of our Ge sample (see chapter 3), $w \sim 133nm$ and TE regime is the dominating one [5]. In this case, the intensity current is given by [4,5]:

$$I = AA^*T^2 e^{-\varphi_B/k_bT}\left(e^{qV/\eta k_bT} - 1\right), \tag{1.1.4}$$

where $A^* = 4\pi m_e^* k_b^2 q/h^3 = 120\frac{m_e^*}{m_e} Acm^{-2}K^{-2}$ [5]. A is the area of the junction, m_e^* is the electron effective mass, whereas η is the ideality factor, taking into accounts all the effects that make the device not ideal, such as Fermi level pinning and others[4].

1.2 Graphene/semiconductor Schottky junction

Fig. 1.3 (b) shows the conduction and valence band for graphene plotted in the first Brillouin zone, obtained by tight-binding calculations [27]. The two bands touch in six points of the Brillouin zone, the Dirac points, which correspond to the six vertices of a hexagon (Fig 1.3 (a)). The six Dirac points of a unit cell can be reduced

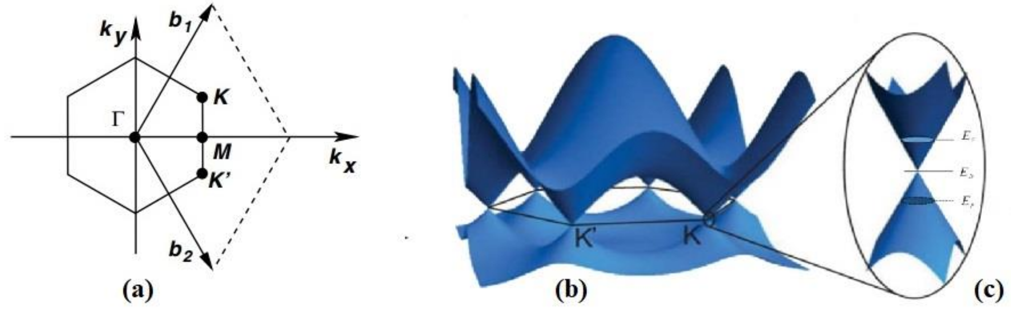

Fig. 1.3 ***(a)*** *First Brillouin zone in reciprocal space.* $\boldsymbol{b}_1$ and $\boldsymbol{b}_2$ *are the generators of the reciprocal lattice. The six corners of the hexagonal Brillouin zone are the Dirac points, K and K' are the two non-equivalent points. Figure adapted from Ref. [24].* ***(b)*** *conduction (top) and valence (down) band in the first Brillouin zone. It can be seen that the two bands are symmetric.* ***(c)*** *Dirac cones at the K point. Figure adapted from Ref. [4].*

to two inequivalent sets of three points, labelled as K and K', where the points of each set are equivalent by symmetry. Since the CB and the VB touch at the Dirac points, graphene is a zero-gap semiconductor (semimetal). At $T = 0K$, the valence band is completely filled, and the conduction band is completely empty [27], with the Fermi level lying at the Dirac points. At finite temperature, thanks to the zero gap, electrons are thermally excited in the conduction band and graphene becomes conductive. Moreover, near the Dirac points, conduction and valence bands show a linear dependence on the wavevector, forming two symmetric cones called Dirac cones (Fig. 1.3 (c)) described by the equation [28]:

$$E_{\pm} = \pm \hbar v_F |\boldsymbol{q}|, \tag{1.2.1}$$

where $\pm$ stands for conduction and valence band respectively, $\boldsymbol{q} = \boldsymbol{k} - \boldsymbol{K}$ (or $\boldsymbol{q} = \boldsymbol{k} - \boldsymbol{K}'$), and $v_F \approx 10^6 m/s$ [4,30,31]. Eq. (1.2.1) gives to the eigenvalues of the Dirac equation for massless particle [28] with a constant velocity v_F. Carriers travel in graphene as they lose their mass and therefore are usually referred to as Dirac fermions. Each Brillouin zone contains two non-equivalent Dirac cones, giving rise to a double valley degeneracy.

The linear dispersion relation at the Dirac cones also gives a linear density of states (DOS), given by the equation (taking in considerations both spin and valley degeneracy) [27]:

$$DOS(E) = \frac{2}{\pi} \frac{1}{(\hbar v_F)^2} |E|. \tag{1.2.2}$$

Since graphene is a semi-metal, when it is brought into contact with a semiconductor, a Schottky junction is formed. A complete understanding of the Schottky barrier formation in graphene/SC heterostructures has not been yet reached [4]: the main challenge here is due to the mismatch dimensionality between 2D graphene and the 3D semiconductor. L. Hu et Al. [7] pointed out that the SBH in graphene/3D semiconductor junction is strongly dependent on the atomic structure at the interface, showing a low correlation with the semiconductor work function. Moreover, in these systems, also Fermi level pinning takes place [7].

The main difference that arises with respect to standard M/SC junction is that, as mentioned before, due to the finite density of states in graphene at the Dirac point, φ_B is bias-dependent in graphene/SC Schottky junctions is bias-dependent. Indeed, using Eq. (1.2.1), the density of electrons per unit area (at $T = 0$ K, for simplicity) is given by:

$$n = \int_0^{\infty} DOS(E) f(E) dE = \left(\frac{2\sqrt{\pi}}{h v_F}\right)^2 E_F^2, \tag{1.2.3}$$

where f (E) is the Fermi-Dirac distribution. When a graphene/n-SC junction is formed, the positive charge in the depletion region of the semiconductor is balanced by an equivalent but opposite charge in graphene layer, which is created by moving the graphene Fermi level. From Eq. (1.2.2), the relation between Fermi level and carrier density in graphene is:

$$E_F = \frac{h v_F}{2\sqrt{\pi}} \sqrt{|n|}, \tag{1.2.4}$$

which corresponds to an energy shift of 0.47eV for a transfer of 0.01 electron per unit cell [4]. With respect to the Dirac point, $E_F > 0$ (< 0) for electrons (holes). When a bias V is applied, according to Eq. (1.1.3) the charge induced in graphene is:

$$Q_g(V) = -Q_S(V) = -qN_D A w = -qA\sqrt{\frac{2\varepsilon_S N_D}{q^2}(\varphi_{bi} - qV - k_B T)}\,, \tag{1.2.5}$$

where Q_S is the charge in the depletion region of the semiconductor. In forward bias ($V > 0$), the positive pole is applied at the graphene side of the junction while in reverse ($V < 0$) is applied at the metal side. By dividing for $-q$ and A we obtain the corresponding electrons surface density:

$$n_g(V) = n_0 + \Delta n = \sqrt{\frac{2\varepsilon_S N_D}{q^2}(\varphi_{bi} - qV - k_B T)} \tag{1.2.6}$$

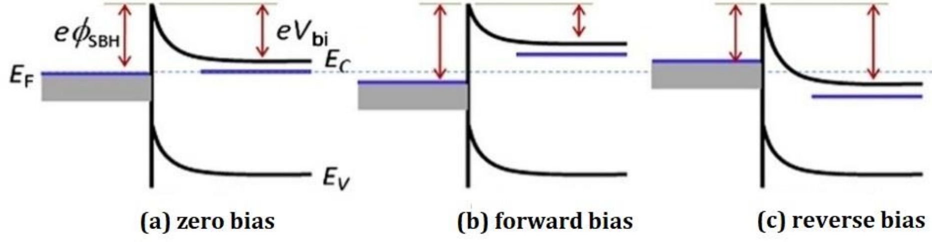

Fig. 1.4 *Fermi level shift and associated φ_B shift in graphene/SC junction. **(a)** zero bias; **(b)** forward bias: φ_B increases; **(c)** reverse bias, φ_B decreases. Figure adapted from Ref. [22].*

where n_0 is the initial natural *p*-doping of graphene, which arises usually from air contamination [4,25]. Therefore, from Eq. (1.2.4), the Fermi level shift is:

$$\Delta E_F(V) = E_F(V) - E_F(0) = \frac{h v_F}{2\sqrt{\pi}}\left(\sqrt{n_0 + \Delta n} - \sqrt{n_0}\right). \tag{1.2.7}$$

Under the assumption $n_0 \gg \Delta n$ [4,25], we finally get:

$$\Delta E_F(V) = \frac{h v_F}{4\sqrt{\pi}}\sqrt{\frac{2\varepsilon_S N_D}{n_0 q^2}}\left(\sqrt{\varphi_{bi} - qV - k_B T} - \sqrt{\varphi_{bi} - k_B T}\,\right). \tag{1.2.8}$$

The variation of the SBH is the opposite of the variation of the Fermi level (Fig. 1.4), $\Delta\varphi_B = -\Delta E_F$. If we call $\varphi_{B,0}$ the zero bias SBH and we insert the voltage dependent correction in the equation for TE, we get:

$$I = AA^* T^2 e^{-[\varphi_{B,0} - a(\sqrt{\varphi_{bi} - qV} - \sqrt{\varphi_{bi}}\,)]/k_b T}\left(e^{qV/\eta k_b T} - 1\right)$$

$$= I_s(V)\left(e^{qV/\eta k_b T} - 1\right), \tag{1.2.9}$$

where $a = \frac{h v_F}{4\sqrt{\pi}}\sqrt{\frac{2\varepsilon_S N_D}{n_0 q^2}}$. The SBH is increased in forward bias (Fig. 1.4 (b)), while it is lowered when reverse bias is applied (Fig. 1.4 (c)). In forward regime, the Fermi level shift cannot be distinguished from voltage drop associated to the series resistance of the diode, which are important at large currents. On the contrary, the effect is evident in reverse bias, where a clear voltage dependent current can be observed, in contrast with traditional metal/SC junctions which show a constant saturation current [22].

S. Liang et Al. [7,8] have proposed a modified expression for TE emission if graphene is used in Schottky contact instead of metals. The modified model tries to explain the low experimental values of A^* and to overcome theoretical issues regarding the effective mass dependence of the Richardson constant, which is

contrast with the massless behaviour of electrons in the Dirac cones. A modified diode equation for thermionic emission in graphene/SC junctions can be written as:

$$I = AA^{*}T^{3}e^{-\frac{\varphi_{B}-E_{F}(V)}{k_{b}T}}\left[e^{\frac{qV}{\eta k_{b}T}}-1\right], \tag{1.2.10}$$

where $A^{*} = 8\pi^{2}k_{b}^{3}q/h^{3}v_{F}^{2} = 0.001158\frac{A}{cm^{2}}$. This formula also takes into accounts the bias-tuneable Fermi level.

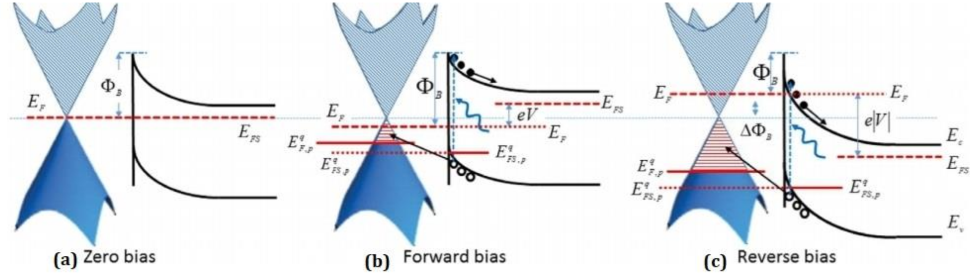

Fig.1.5 *Band diagrams of graphene/SC junction in case of* ***(a)*** *darkness under zero bias;* ***(b)*** *illumination under forward bias;* ***(c)*** *illumination under reverse bias. Figure adapted from Ref.[4]*

1.3 Light -Graphene/SC interaction

Graphene/SC junctions find a wide application in photonic devices (LEDs, solar cell, photodetectors etc.) [6] where high conductivity and low absorption of graphene in near infrared (NIR)-violet range (≈ 2.3%) make it an ideal candidate as an almost transparent electrode. In photodetectors application, almost all the impinging light is therefore absorbed by the semiconductor, where it generates electrons-holes couples, which are then injected in graphene by the built-in potential, where they show a much higher lifetime than if they were directly generated in graphene [4]. A remarkable difference with respect to M/SC photodiode is that the photocurrent drops to zero as the bias approaches the forward regime, for a sufficiently high impinging power (≈1μW in graphene/Si) [23], resulting in non-open circuit photovoltage. This effect is once again due to the finite density of states of graphene. Indeed, photogenerated holes are injected by the built-in potential into graphene, where they rearrange according to the holes quasi-Fermi level in graphene $E_{F,p}^{q}$. This level lies below the charge neutrality point and cannot be lower than the holes quasi-Fermi level in the semiconductor $E_{FS,p}^{q}$, which is set by the impinging light power [26,4]. Under forward bias, the Fermi level in the

semiconductor E_{FS}, and so $E_{FS,p}^{q}$, are pushed upward with respect to the charge neutrality point (Fig. 1.5 (b)), limiting the accessible holes states in graphene and therefore suppressing the photocurrent. In reverse bias (Fig.1.5 (c)), the effect is the opposite: for sufficiently high reverse bias, photogenerated holes can be injected into graphene and the photocurrent rapidly reaches the saturation level (Fig. 1.6).

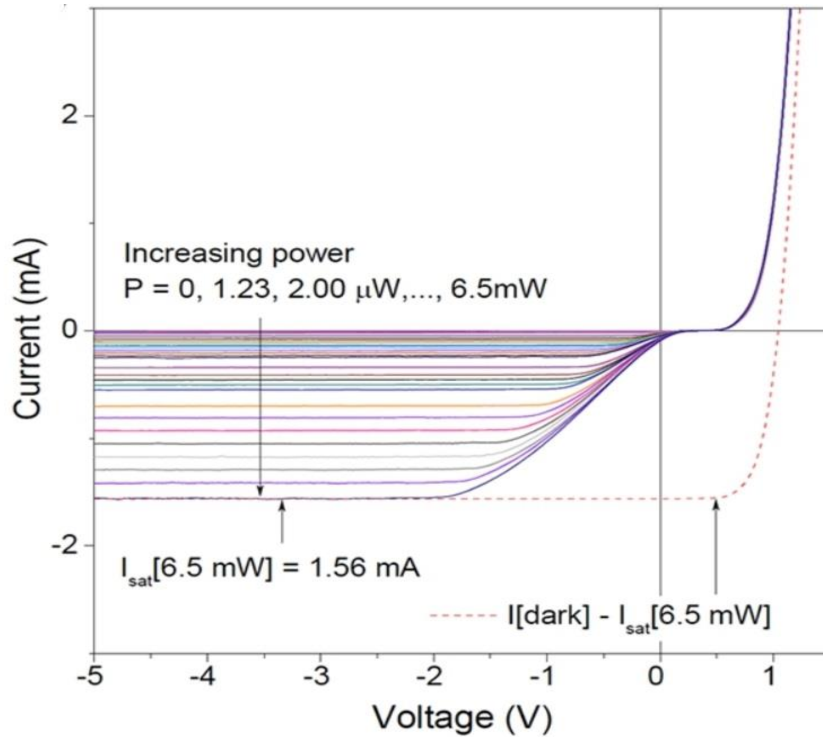

Fig. 1.6 *I-V curve for a graphene/n-Si junction for different incident power. The dashed line represents the ideal photodiode behaviour at P=1.65mW. It is evident the photocurrent drops as bias approaches the forward regime. Figure adapted from Ref. [23].*

Chapter 2

Photoinduced Inverse Spin-Hall Effect

The following chapter first deals with the photogeneration of spin polarized electrons in semiconductors by means of illumination with circularly polarized light (CPL), a phenomenon known as *optical orientation*. The latter is first introduced in the case of a general direct gap semiconductor and then in the particular case of Ge.

Spin currents flowing in semiconductors can be detected by means of inverse spin-Hall effect (ISHE) in non-magnetic heavy metals [14], which converts a spin current into an electromotive force. ISHE detectors can be realized by deposition of a thin layer of non-magnetic heavy metal, typically Pt, on top of the semiconductor [9-13]. ISHE is introduced in section 2.2, with particular aim on the characteristic dependences of ISHE signal, which have been exploited during the experimental part of the thesis (see chapter 5).

As shown by K.Ando [9], the combination of optical orientation in semiconductors and ISHE allows for the conversion of light polarization information into an electric signal, with the possibility of integration of spintronics on semiconductors with photonics applications [9].

2.1 Spin optical orientation in direct gap semiconductor

Optical orientation is a well-known technique used to generate spin polarized carriers in direct gap semiconductors under illumination with CPL [9,22]. A right (left) circularly polarized photon carries an angular momentum with a projection along the direction parallel to the wave vector equal to +1 (-1) (in unit of ħ). When this photon is absorbed in an inter-band transition, its angular momentum is distributed between the excited electrons in the conduction band and the holes in

the valence band [25]. Thanks to the dipole selection rules, if the absorption takes place in a direct gap semiconductor, the excited carriers will have a net spin polarization given by

$$\boldsymbol{P} = (n_\uparrow - n_\downarrow)/(n_\uparrow + n_\downarrow)\boldsymbol{u_k}, \tag{2.1.1}$$

where $n_\uparrow$ ($n_\downarrow$) is the density of carriers with spin parallel (anti-parallel) with respect to the quantization axis, given by the direction of the incident light (parallel to $\boldsymbol{u}_\mathbf{k}$). Since spin lifetime for holes is much shorter the spin lifetime for electrons (100 fs vs 35 ps in GaAs [9], nanoseconds vs few hundreds of femtoseconds in Ge [12]) spin transport phenomena in these systems are mainly due to photoexcited electrons. Therefore, from now on, I will only focus on electrons. In order to understand how selection rules work in the optical orientation process, it is important to understand how the conduction and valence bands are made in direct gap semiconductors.

2.1.1 Conduction and valence band in direct gap semiconductors

The band structure of a semiconductor can be calculated using the tight binding (TB) method, where the atomic orbitals are combined to form the eigenstates describing the valence electrons in the crystal [32]. In order to understand the role of atomic orbitals in the formation of conduction and valence bands in semiconductors, let us first consider a simple 1D periodic chain of atoms, equally spaced by a distance a (Fig. 2.1). In the frame of TB, the crystal wavefunction can be written as follow:

$$\Psi_{\boldsymbol{k}} = \sum_{\boldsymbol{R}} \sum_j e^{i\boldsymbol{k}\cdot\boldsymbol{R}} \alpha_j \varphi_j(\boldsymbol{r} - \boldsymbol{R}) = \sum_{\boldsymbol{R}} e^{i\boldsymbol{k}\cdot\boldsymbol{R}} \varphi(\boldsymbol{r} - \boldsymbol{R}). \tag{2.1.1}$$

This equation is given by the overlap of functions $\varphi(\boldsymbol{r} - \boldsymbol{R})$, each localized on the atom in the position $\boldsymbol{R} = n\boldsymbol{a}$, modulated by the phase $e^{i\boldsymbol{k}\cdot\boldsymbol{R}}$. This phase term allows Eq. (2.1.1) respecting the Bloch theorem: $\Psi_{\boldsymbol{k}}(\boldsymbol{r} + \boldsymbol{R}) = \Psi_{\boldsymbol{k}}(\boldsymbol{r})e^{i\boldsymbol{k}\cdot\boldsymbol{R}}$. The sum is performed over all the lattice vectors $\boldsymbol{R}$, while $\boldsymbol{k}$ varies in the first Brillouin zone (so $-\pi/a < \boldsymbol{k} < \pi/a$ for the 1D chain). The function $\varphi(\boldsymbol{r})$ is given by a linear combination of the atomic orbitals labelled by j, each weighted by the term α_j.Since atomic orbitals form a complete set of orthonormal functions, to obtain a correct expression for $\Psi_{\boldsymbol{k}}$ the index j should extend over all the atomic orbitals. In practice, the sum can be limited to the valence atomic orbitals, since they are the only one which give an appreciable overlap.

In order to find the correct eigenfunctions and eigenvalues, Eq. (2.1.1) has to be plug into the 1D Schrodinger equation:

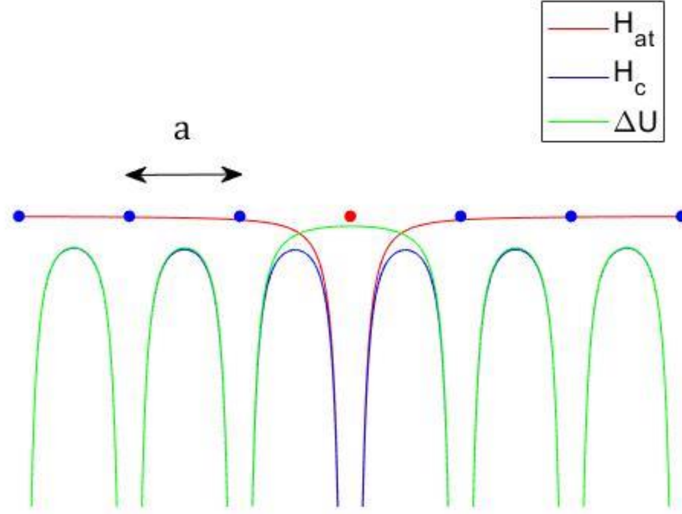

Fig. 2.1 *1D chain of atoms separated by a distance* a*. The origin is placed on the atomic site indicated by the red dot. The blue curve shows the behaviour of the periodic crystal potential, the red curve is the atomic potential of the atom centred in the origin and the green curve is the perturbation term ΔU(r).*

$$H_c(\boldsymbol{r})\Psi_{\boldsymbol{k}} = \varepsilon(\boldsymbol{k})\Psi_{\boldsymbol{k}}. \tag{2.1.2}$$

The crystal potential H_c (blue line in Fig. 2.1) can be seen as a series of Coulomb potentials, each centred on each lattice site. Assuming that each Coulomb potential is well localized near each atom, H_c at a given lattice point can be approximated by the atomic potential H_{at} in that site (red line in Fig. 2.1) plus a correction ΔU (green line in Fig. 2.1) with the symmetry of the crystal. Therefore, Eq. (2.1.2) at the origin becomes:

$$H_c(\boldsymbol{r}) = H_{at}(\boldsymbol{r}) + \Delta U(\boldsymbol{r}). \tag{2.1.3}$$

Let us now assume that valence orbitals for the atoms of our chain are only s type orbitals. Under this approximation, using Eq. (2.1.1) and Eq. (2.1.3), Eq. (2.1.2) becomes [32]:

$$\left(H_{at}(r) + \Delta U(r)\right) \sum_R e^{ikr} \varphi_s(r - R) = \varepsilon(k) \sum_R e^{ikr} \varphi_s(r - R), \tag{2.1.4}$$

where now scalar values for k, r and R have been considered. Eq. (2.1.4) can be solved by left multiplication of $\langle \varphi_s(r)|$. In *bra-ket* notation:

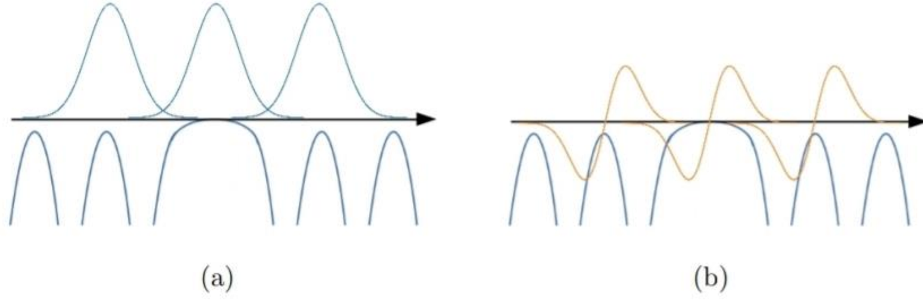

Fig. 2.2 *Schematic rapresentation of overlap integral in case of* ***(a)*** *s-type orbitlas and* ***(b)*** *p-type orbitals. Figure adapted from Ref. [37].*

$$\langle\varphi_s(r)|H_{at}|\varphi_s(r)\rangle + \sum_{R\neq 0} e^{ikR}\langle\varphi_s(r)|H_{at}|\varphi_s(r-R)\rangle + \langle\varphi_s(r)|\Delta U(r)|\varphi_s(r)\rangle + \sum_{R\neq 0} e^{ikR}\langle\varphi_s(r)|\Delta U(r)|\varphi_s(r-R)\rangle = \varepsilon(k)\langle\varphi_s(r)|\varphi_s(r)\rangle + \varepsilon(k)\sum_{R\neq 0} e^{ikR}\langle\varphi_s(r)|\varphi_s(r-R)\rangle. \quad (2.1.5)$$

Since $\varphi_s(r)$ is an eigenfunction of H_{at}, with eigenvalue ε_s, and since $\langle\varphi_s(r)|\varphi_s(r)\rangle = 1$, Eq. (2.1.5) becomes:

$$\varepsilon_s\left[1 + \sum_{R\neq 0} e^{ikR}\alpha(R)\right] - \beta - \sum_{R\neq 0} e^{ikR}\gamma(R) = \varepsilon(k)\left[1 + \sum_{R\neq 0} e^{ikR}\alpha(R)\right], \quad (2.1.6)$$

where:

$$\alpha(R) = \langle\varphi_s(r)|\varphi_s(r-R)\rangle \quad (2.1.7)$$

$$\beta = -\langle\varphi_s(r)|\Delta U(r)|\varphi_s(r)\rangle \quad (2.1.8)$$

$$\gamma(R) = -\langle\varphi_s(r)|\Delta U(r)|\varphi_s(r-R)\rangle. \quad (2.1.9)$$

γ is the overlap integral between the atomic wavefunctions on two different sites, mediated by ΔU. Its value can be considered significantly different from zero only when it is evaluated between nearest neighbours, so for values of $R = \pm a$. The term α is the orthogonality factor. This term can be neglected also for nearest neighbours, assuming a very small overlap between the atomic wavefunctions when the overlap is not mediated by ΔU. For a more precise solution, α can be set to zero using the Löwdin orthogonalization, which properly combine $\varphi_s(r-R)$ to make them orthogonal. The drawback of this method is that ε_s is no more the *s*-level eigenvalue of the isolated atom, but it is a parameter which need to be fit experimentally [33]. Having said that, the eigenvalue $\varepsilon(k)$ can be expressed as:

$$\varepsilon(k) = \varepsilon_s - \beta - 2\gamma\cos(ka), \tag{2.1.10}$$

where it has been used the fact that $\gamma(a) = \gamma(-a) = \gamma$, since φ_s and ΔU are both even. Near the centre of the first Brillouin zone, $ka \ll 1$ and the *cos* term can be expanded. Eq. (2.1.10) takes the form:

$$\varepsilon(k) \propto \gamma a^2 k^2 = \hbar^2 k^2 / 2m_{eff}, \tag{2.1.11}$$

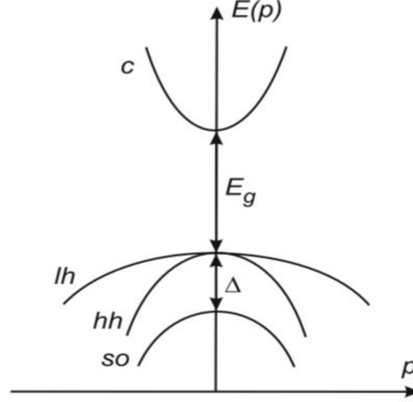

***Fig. 2.3** Conduction and valence band for a direct gap semiconductor (GaAs) in the presence of a relevant spin-orbit coupling. Figure adapted from Ref [19].*

where $m_{eff} = \hbar^2/2\gamma a^2$. The overlap between *s*-type orbitals is positive (Fig. 2.2 (a)) and since $\Delta U < 0$, the bracket term in Eq. (2.1.9) is negative. Therefore $\gamma > 0$, giving a minimum in the band structure at Γ. Instead, if *p*-like orbitals were used, the overlap between *p*-type orbitals would be negative (Fig. 2.2 (b)) and so $\gamma < 0$: $\varepsilon(k)$ would now have a maximum at Γ. Despite the simplicity of the 1D model, the *s*-type (*p*-type) symmetry of the states at minima (maxima) of the band-structure at Γ is a general feature which is also valid for real 3D semiconductors. In that case, the orbital atoms that need to be used in Eq. (2.1.1) are *s*, p_x, p_y, and p_z. The conduction and valence bands for a direct gap semiconductor at Γ are shown in Fig. 2.3. The following features are valid:

- CONDUCTION BAND: states at the bottom of the conduction band have *s*-type symmetry and are doubly degenerate by spin. The wavefunction for an electron in CB in the vicinity of Γcan be written as [25]:
  $\Psi_{\boldsymbol{k}m} = u_m e^{i\boldsymbol{k}\cdot\boldsymbol{r}}$, $m = \pm 1/2$ with
  $$u_{1/2} = S|\uparrow\rangle \text{ , } u_{-1/2} = S|\downarrow\rangle. \tag{2.1.12}$$
  S is the *s*-type Bloch amplitude and transforms as an eigenfunction of $\hat{L}^2$and $\hat{L}_z$, with quantum numbers $l = m_l = 0$. $|\uparrow\rangle$ ($|\downarrow\rangle$) is the 2-dimensional spinor

corresponding to a spin oriented parallel (anti-parallel) with respect to an arbitrary z-axis.

- VALENCE BAND: states at the top of the valence band have *p*-type symmetry since are formed combining p_x, p_y, and p_z orbitals. Therefore, electrons carry a net orbital momentum with quantum number $l = 1$, which is coupled with the spin component of the angular momentum by the spin-orbit (SO) interaction [33]:
$$\hat{H}_{SO} = {}^{\Delta}/_{3}\,\hat{\boldsymbol{L}} \cdot \hat{\boldsymbol{S}} = \frac{\Delta}{3}\frac{1}{2}(\hat{J}^2 - \hat{L}^2 - \hat{S}^2), \tag{2.1.13}$$
where $\hat{\boldsymbol{J}} = \hat{\boldsymbol{L}} + \hat{\boldsymbol{S}}$ is the total angular momentum. The first consequence of SO is that now the Hamiltonian does not longer commute with $\hat{\boldsymbol{L}}$ and $\hat{\boldsymbol{S}}$, while it commutes with $\hat{\boldsymbol{J}}$ (the orbital and the spin part of the angular momentum are no longer separately conserved, while it is conserved the total angular momentum). The eigenstates at the top of the valence band are obtained combining the orbital part of the wavefunction (made by combination of p_x, p_y, and p_z orbitals) with the spin part, in order to obtain states that transforms as eigenstates of $\hat{J}^2$ and $\hat{J}_z$, with orbital quantum number $j = 3/2, 1/2$. The correct combination is obtain using the Clebsh-Gordan technique, whose results for CB and VB states at Γ are reported in Table 2.1. Using these new eigenstates, the first order correction in energy given by SO is:
$$\langle H_{SO} \rangle = \frac{\Delta}{6}(j(j+1) - l(l+1) - s(s+1). \tag{2.1.14}$$
For $l = 1$ and $s = 1/2$, j can take values of $1/2$ or $3/2$. By substituting the values for *s, l* and *j* in Eq. (2.1.14), SO splits the valence band states with $j = 3/2$ from the valence bands states with $j = 1/2$ at Γ by a quantity *Δ*. The former can be further divided in to 4 bands with $m_j = \pm 3/2, \pm 1/2$, which are the heavy hole (HH) and the light hole (LH) states, respectively. These four states are degenerate at the centre of the Brillouin zone, while for $\boldsymbol{k} \neq 0$ the degeneracy between HH and LH is removed (Fig. 2.3). The states with $j = 1/2$ form a two-fold degenerate bands with $m_j = \pm 1/2$, the split-off band. The spin-orbit coupling scales in intensity as Z^4, where *Z* is the atomic number. Therefore, it is quite weak in light semiconductor, like Si, while it plays a relevant role in heavier semiconductors like Ge or GaAs.

The behaviour of HH and LH bands for $\boldsymbol{k} \neq 0$ and for $E(\boldsymbol{k}) \ll \Delta$ can be studied using the Luttinger Hamiltonian. Under spherical approximation, the Luttinger Hamiltonian can be built from symmetry considerations, combining the momentum operator $\boldsymbol{p}$ with the total angular momentum operator $\boldsymbol{J}$ in order to obtain a scalar Hamiltonian which is invariant under arbitrary rotations [19]:

Band	$\vert j, m_j\rangle$	Ψ
CB	$\vert 1/2, 1/2\rangle$ $\vert -1/2, -1/2\rangle$	$\vert s\rangle\vert\uparrow\rangle$ $\vert s\rangle\vert\downarrow\rangle$
HH	$\vert 3/2, 3/2\rangle$ $\vert 3/2, -3/2\rangle$	$-1/\sqrt{2}\vert p_x + ip_y\rangle\vert\uparrow\rangle$ $1/\sqrt{2}\vert p_x - ip_y\rangle\vert\downarrow\rangle$
LH	$\vert 3/2, 1/2\rangle$ $\vert 3/2, -1/2\rangle$	$-1/\sqrt{6}(\ \vert p_x + ip_y\rangle\vert\downarrow\rangle - 2\vert p_z\rangle\vert\uparrow\rangle\ )$ $1/\sqrt{6}(\ \vert p_x - ip_y\rangle\vert\uparrow\rangle - 2\vert p_z\rangle\vert\downarrow\rangle\ )$
SO	$\vert 1/2, 1/2\rangle$ $\vert 1/2, -1/2\rangle$	$-1/\sqrt{3}(\ \vert p_x + ip_y\rangle\vert\downarrow\rangle + \vert p_z\rangle\vert\uparrow\rangle\ )$ $-1/\sqrt{3}(\ \vert p_x - ip_y\rangle\vert\uparrow\rangle - \vert p_z\rangle\vert\downarrow\rangle\ )$

Table 2.1 *Clebsh-Gordan integrals for CB and VB states at Γ. Ref. [30].*

$$H_L = Ap^2 I + B(\boldsymbol{p} \cdot \boldsymbol{J})^2. \quad (2.1.15)$$

For $j = 3/2$, which is the case for HH and LH bands, I is the 4×4 identity matrix and $\boldsymbol{J}$ is a set of 4×4 matrixes J_x, J_y and J_z, where J_z is a diagonal matrix with eigenvalues $-\frac{3}{2}, -\frac{1}{2}, \frac{1}{2}$ and $\frac{3}{2}$. A and B are arbitrary constants. The energy spectrum for the HH and LH can be obtained diagonalizing Eq. (2.1.15). Since the choice of *x,y,* and *z* axis is arbitrary, one can chose the *z*-axis parallel to $\boldsymbol{p}$, simplifying the calculations. The diagonalization of Eq. (2.1.15) gives:

$$E_h(p) = \left(A + \frac{9}{4}B\right)p^2 = \frac{p^2}{2m_h} \quad J_z = \pm\frac{3}{2}, \quad (2.1.16)$$

$$E_l(p) = \left(A + \frac{1}{4}B\right)p^2 = \frac{p^2}{2m_l} \quad J_z = \pm\frac{1}{2}. \quad (2.1.17)$$

Normally $B < 0$, while $A + \frac{9}{4}B > 0$ [19], so both masses are positive. There are two degenerate HH bands, with a projection of $\boldsymbol{J}$ on the direction of $\boldsymbol{p}$ of $= \pm\frac{3}{2}$ and two degenerate LH bands, with a projection of of $\boldsymbol{J}$ on the direction of $\boldsymbol{p}$ of $= \pm\frac{1}{2}$. These bands are degenerate at Γ, where $\boldsymbol{p} = 0$, while for $\boldsymbol{p} \neq 0$ the degeneracy is removed and HH and LH have different parabolic dispersions.

Although spherical approximation simplifies the calculations, a more complete form of the Luttinger Hamiltonian should take in consideration the cubic symmetry of the systems. The choice of *x, y* and *z* axes is no more arbitrary, but they coincide with the crystallographic axes of the cubic system. Eq. (2.1.16) then takes the form [19]:

$$H_L = Ap^2 I + B(\boldsymbol{p} \cdot \boldsymbol{J})^2 + C(J_x p_x^2 + J_y p_y^2 + J_z p_z^2). \quad (2.1.18)$$

The last term of Eq. (2.1.18) makes the isoenergetic surfaces of light and heavy holes band anisotropic, so that $E_h(\boldsymbol{p})$ and $E_l(\boldsymbol{p})$ do not have a simple parabolic dispersion.

2.1.2 Interaction with circularly polarized light

The transition rate for an optical direct transition between an initial and final state is given by the Fermi golden rule. In the frame of the electric dipole approximation, it takes the form [33]:

$$W_{if} = \frac{2\pi}{\hbar}\left(\frac{qE_0}{m\omega}\right)^2 \left|\boldsymbol{e}\cdot\langle f|\widehat{\boldsymbol{p}}e^{i\boldsymbol{k}_{opt}\cdot\boldsymbol{r}}|i\rangle\right|^2 \delta(E_i - E_f - \hbar\omega), \tag{2.1.19}$$

where E_0 is the amplitude of the incoming electric field, ω and $\boldsymbol{k}_{\text{opt}}$ are the angular frequency and the wave vector of the radiation, $\boldsymbol{e}$ is a unit vector which gives the electric field polarization and $\widehat{\boldsymbol{p}} = -i\hbar\boldsymbol{\nabla}$ is the momentum operator. E_i and E_f are the energies of the initial and final states respectively. In the case of an inter-band transition in a solid, the states $|i\rangle$ and $|f\rangle$ take the form of Bloch wavefunctions for two different bands. The bra-ket term of Eq. (2.1.19) can be rewritten as:

$$-i\hbar\int d\boldsymbol{r}\, u_f^* e^{-i\boldsymbol{k}_f\cdot\boldsymbol{r}} e^{i\boldsymbol{k}_{opt}\cdot\boldsymbol{r}}\, \boldsymbol{\nabla}\left(u_i e^{-i\boldsymbol{k}_i\cdot\boldsymbol{r}}\right) = -i\hbar\int d\boldsymbol{r} e^{i(\boldsymbol{k}_i+\boldsymbol{k}_{opt}-\boldsymbol{k}_f)\cdot\boldsymbol{r}}\, u_f^*\boldsymbol{\nabla}u_i - \hbar\int d\boldsymbol{r} e^{i(\boldsymbol{k}_i+\boldsymbol{k}_{opt}-\boldsymbol{k}_f)\cdot\boldsymbol{r}}\, u_f^* u_i\,. \tag{2.1.20}$$

Since the term $e^{i(\boldsymbol{k}_i+\boldsymbol{k}_{opt}-\boldsymbol{k}_f)\cdot\boldsymbol{r}}$ oscillates very rapidly with $\boldsymbol{r}$, the integral in Eq. (2.1.20) is zero unless

$$\boldsymbol{k}_i + \boldsymbol{k}_{opt} - \boldsymbol{k}_f = 0, \tag{2.1.21}$$

which gives the conservation of the total momentum. However, for photon energies up to soft X-rays, $\boldsymbol{k}_{opt}$ is small compare with the size of the first Brillouin zone. Indeed, for $\lambda \gg a$, where a is the lattice constant, of the order of few Å, $2\pi/\lambda \ll 2\pi/a$ and Eq. (2.1.21) can be written as:

$$\boldsymbol{k}_i = \boldsymbol{k}_f, \tag{2.1.22}$$

which is the condition for vertical transition [33]. Given Eq. (2.1.22) and considering that $\langle u_f|u_i\rangle = 0$, since the functions u_j are orthonormal for different bands, Eq. (2.1.19) becomes:

$$W_{if} = \frac{2\pi}{\hbar}\left(\frac{qE_0}{m\omega}\right)^2 \left|\boldsymbol{e}\cdot\langle u_f|\boldsymbol{p}|u_i\rangle\right|^2 \delta(E_i - E_f - \hbar\omega). \tag{2.1.23}$$

Let us now consider an interaction between a direct gap semiconductor and a circularly polarized photon with an energy resonant with the direct gap of the

semiconductor. $\delta(E_i - E_f - \hbar\omega)$ implies that the levels involved are the top of the valence band and the bottom of the conduction of band. Moreover, the spin is not involved in Eq. (2.1.23), so the total spin must be conserved in the transition. For a CPL propagating along the z direction, $\boldsymbol{e}$ takes the form:

$$\boldsymbol{e} = \boldsymbol{e}_x \pm i\boldsymbol{e}_y, \tag{2.1.24}$$

where + (-) is for right (left) circular polarization. If we use right circularly polarized photons (RCP), carrying an angular momentum of +1 (in units of ħ) parallel to the z axis, the possible transitions resonant with the direct gap which respect the total spin conservation are:

$$\Gamma_{HH\to CB}\colon \left|\tfrac{3}{2}, -\tfrac{3}{2}\right\rangle \to |s, \downarrow\rangle,$$

$$\Gamma_{LH\to CB}\colon \left|\tfrac{3}{2}, -\tfrac{1}{2}\right\rangle \to |s, \uparrow\rangle.$$

Using the Clebsh-Gordan integrals of tables 2.1 and Eq. (2.1.24), we have for $\left|\tfrac{3}{2}, -\tfrac{3}{2}\right\rangle \to |s, \downarrow\rangle$:

$$W_{HH\to CB} \propto \left|(\boldsymbol{e}_x + i\boldsymbol{e}_y)\cdot\left\langle s\downarrow\left|-i\hbar\boldsymbol{\nabla}\right|\frac{1}{\sqrt{2}}(p_x - ip_y)\downarrow\right\rangle\right|^2 =$$

$$\left|\frac{1}{\sqrt{2}}\langle s|-i\hbar\partial_x|p_x\rangle + \frac{1}{\sqrt{2}}\langle s|-i\hbar\partial_y|p_y\rangle\right|^2 = 2|p_{cv}|^2, \tag{2.1.25}$$

where it has been used the fact that $\left\langle s\left|-i\hbar\boldsymbol{\nabla}\right|p_{x_j}\right\rangle = \left\langle s\left|-i\hbar\partial_{x_j}\right|p_{x_j}\right\rangle \boldsymbol{e}_{x_j} = p_{cv}\boldsymbol{e}_{x_j}$ for symmetry reasons [25]. Doing the same for $\left|\tfrac{3}{2}, -\tfrac{1}{2}\right\rangle \to |s, \uparrow\rangle$, we obtain that:

$$W_{LH\to CB} \propto \left|(\boldsymbol{e}_x + i\boldsymbol{e}_y)\cdot\left\langle s\uparrow\left|-i\hbar\boldsymbol{\nabla}\right|\frac{1}{\sqrt{6}}(p_x - ip_y)\uparrow + \frac{2}{\sqrt{6}}p_z\downarrow\right\rangle\right|^2$$

$$= \frac{2}{3}|p_{cv}|^2. \tag{2.1.26}$$

The relative intensity for the transition $\left|\tfrac{3}{2}, -\tfrac{3}{2}\right\rangle \to |s, \downarrow\rangle$ at Γ is then three times larger than that for $\left|\tfrac{3}{2}, -\tfrac{1}{2}\right\rangle \to |s, \uparrow\rangle$. Therefore, for each electron promoted in the CB with spin ↑, there are three electrons with spin ↓, with respect to the z axis. The spin polarization of the electrons excited in the conduction band using RCP, for a transition resonant with the direct gap, is then $P = (1-3)/(1+3) = -0.5$, where the sign – indicates antiparallel polarization. It should be noticed that this treatment

is valid only if the photon energy is resonant with the direct gap and the transition occurs at Γ. For higher photon energies, transition with $\boldsymbol{k} \neq 0$ must be considered and the transition rate can be written as:

$$W_{if} \propto \int d\boldsymbol{k}^3 \frac{1}{8\pi^3} P_{i,f}^2(\boldsymbol{k}) \delta\left(E_i - E_f - \hbar\omega\right) \approx$$

$$P_{i,f}^2(0) \int d\boldsymbol{k}^3 \frac{1}{8\pi^3} \delta\left(E_i - E_f - \hbar\omega\right), \tag{2.1.27}$$

where $P_{i,f}(\boldsymbol{k})$ is the matrix element for a given **k** and $\int d\boldsymbol{k}^3 \frac{1}{8\pi^3} \delta\left(E_i - E_f - \hbar\omega\right)$ is the joint density of states (J-DOS). When the photon energy is equal to spin-ornit splitting Δ, electrons can be excited also from the SO bands. For a RCP, the rate at Γ for the transition $\Gamma_{SO \to CB}$: $\left|\frac{1}{2}, -\frac{1}{2}\right\rangle \to |s, \uparrow\rangle$ can be calculated as:

$$W_{SO \to CB} \propto \left|\left(\boldsymbol{e}_x + i\boldsymbol{e}_y\right) \cdot \left\langle s \uparrow \left| -i\hbar \boldsymbol{\nabla} \right| - \frac{1}{\sqrt{3}}\left(p_x - ip_y\right) \uparrow + \frac{1}{\sqrt{3}} p_z \downarrow \right\rangle\right|^2$$

$$= \frac{4}{3} |p_{cv}|^2. \tag{2.1.28}$$

We can see that the intensity for this transition is twice the intensity for the transition $\Gamma_{LH \to CB}$: $\left|\frac{3}{2}, -\frac{1}{2}\right\rangle \to |s, \uparrow\rangle$. Both these transitions excite spin up electrons in CB, and the sum of their intensities is equal to the intensity of the transition from the HH band, which promotes spin down electrons in the CB. For this reason, the spin polarization drops as the photon energy reaches Δ. Anyway, the weight of each transition is modulated by the JDOS, which is the reason why the polarization, although drops to values lower than 10%, does not drop to zero [26]. The detrimental role of transitions from the SO band to optical orientation is the reason why a large spin orbit coupling is a necessary condition to reach an efficient spin polarization.

Fig. 2.4 shows the transitions that can occur at Γ, with their relative intensities, for RCP and LCP. Using LCP, with similar calculations as done before, it can be shown that it can be reached a polarization $P = 50\%$ for a photon energy resonant with the direct gap.

2.1.3 Optical orientation in Ge

In the previous sections we have seen how the band structure of direct gap semiconductors promote the generation of a spin polarized carriers population upon illumination with circularly polarized light. Recent works [10-13,29,32] have demonstrated that the same result can be obtained using Ge. Ge is an indirect gap

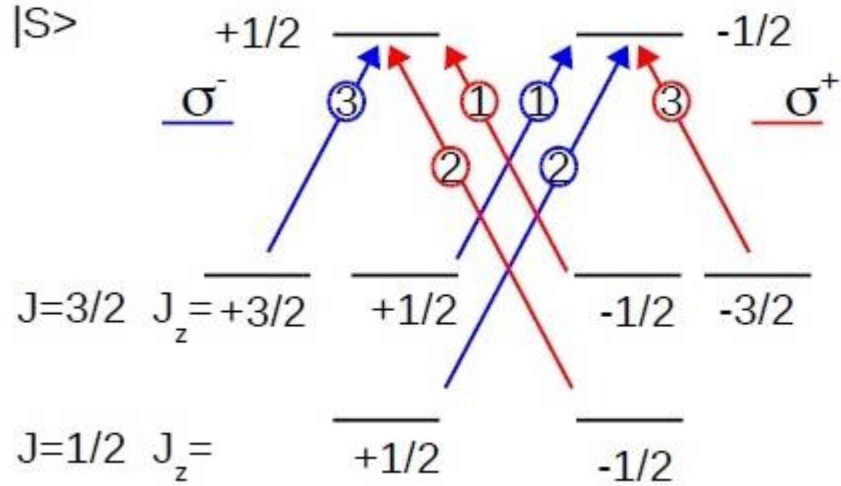

Fig.2.4 *States involved in the direct transition at Γ point and relative strength. Red (blue) arrows show transitions induced by right(left)-circularly polarized light. Values of angular momentum are expressed in unit of ħ. Figure adapted from [37].*

semiconductor, but its band structure near Γ is very similar to that of a III-V direct gap semiconductor, having a relative minimum in the conduction band (Fig. 2.5 (a)). The direct gap $E_g^{\Gamma} = 0.8eV$ is just slightly larger than the indirect gap $E_g^{L} = 0.66eV$ and, since the direct absorption process is much more intense than the phonon assisted absorption at the indirect gap [29], the absorption coefficient for Ge has a net onset at the direct gap. Ge also presents large spin-orbit coupling, which produces a split between the HH-LH bands and the SO bands at Γ of $\Delta = 0.3eV$. These two features make Ge a good candidate for optical orientation, and spin polarization up to $P = 50\%$ can be reached for the excitation at the direct gap. The polarization spectrum as a function of the photon energy can be calculated using the JDOS, as shown in section 2.1.2. Fig. 2.5 (b) shows the result obtained by J. Rioux [26], using the $\boldsymbol{k} \cdot \boldsymbol{p}$ model with a 30-state basis. For energies higher than the direct gap onset, P drops but remains above 40%, as the states in the previous section enter with different weight. At 1.1eV, the photon energy reaches the onset for the absorption from the SO bands. The contribution of transitions from these states and a drop in the polarization from the light-hole mediated transitions reduces the polarization below 10%. Fig. 2.5 (b) also reports the polarization spectrum for holes. As can be seen, it reaches values over than 80% at the onset of the absorption. The reason why we can neglect the holes spin polarization is just because the spin lifetime for holes is much shorter than the electrons spin lifetime, as seen before, so we are allowed to consider holes as unpolarized.

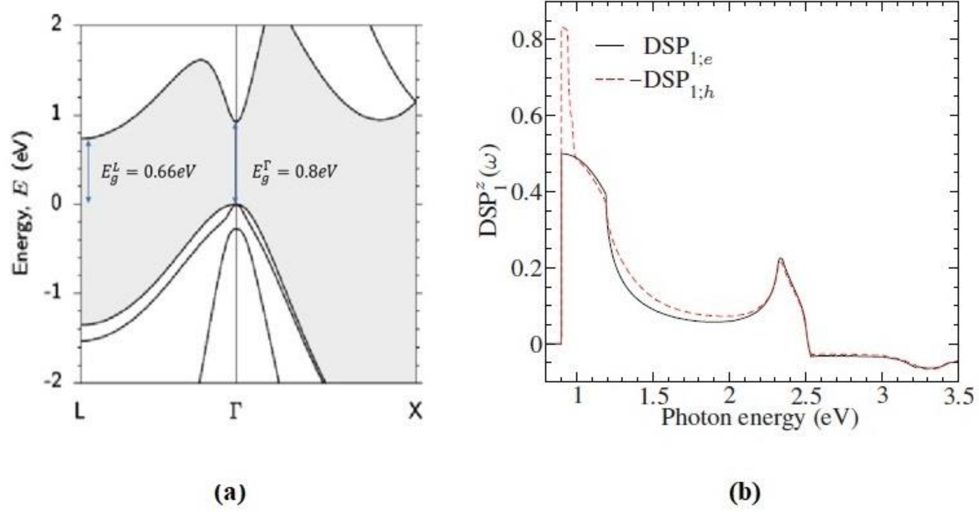

***Fig. 2.5 (a)** Band structure of Ge. Figure adapted from Ref. [36]. **(b)** Degree of spin polarization (DSP) for electrons -black line- and holes -red dashed line- optically injected in Ge by means of LCP light as function of the photon energy. Figure adapted from Ref. [26].*

Once electrons are excited at the top of the conduction band, they rapidly thermalise to the L-valleys within $300\ fs$ [10]. It has been demonstrated that this scattering preserves at least partially the initial spin polarization [10,12,32] and both electrons and spin diffusion is dominated by transport through the long-lived L-states (the electron lifetime at the L-valleys is $\tau_L \approx 1\mu s$).

2.2 Inverse spin-Hall detection

In paramagnetic materials with large atomic numbers, spin-orbit interaction between the elctrons and a scattering target leads to a spin-dependent scattering asymetry with respect to the plain containing the directions of the electron's spin and initial momentum. Electrons with opposite spin polarizations are preferentially scattered in opposite directions producing a spacial separations of opposite spin [14,31]. This penomenon allows for mutual conversion of spin and charge currents and can be used to convert a spin current into a charge current and vice versa.

If we label as $n_{\uparrow,\downarrow}$ the electron density for the spin up and spin down populations, then we can define the electron density and the spin density as follow:

$$n = n_\uparrow + n_\downarrow, \tag{2.2.1}$$

$$s = n_{\uparrow} - n_{\downarrow} = Pn, \tag{2.2.2}$$

where P is the spin polarization. The spin current density is then defined as [20]:

$$\boldsymbol{J}_s = qs\mu\boldsymbol{E} + qD\boldsymbol{\nabla}s, \tag{2.2.3}$$

where μ and D are the mobility and the diffusivity of the carriers.

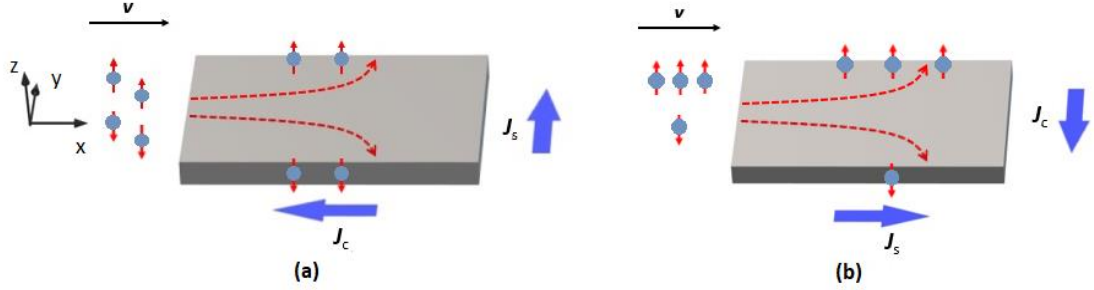

Fig. 2.6 (a) *Spin-Hall effect. An unpolarized current in the x-direction generates a pure spin current on the y-direction and a spin-Hall voltage.* ***(b)*** *Inverse spin-Hall effect. A spin current density J_s in the x-direction generates a charge current density J_c in the y direction and a voltage drop at the edges of the slab.*

Let us consider a flow of electrons travelling along *the x*-direction, with *z* being the good quantization axis for the spin, as shown in Fig. 2.6 (a). Since the number of spin up electrons is equal to the number of spin down electrons, ($n_{\uparrow} = n_{\downarrow}$), $P = 0$ and there is no net spin transport associated to that current. Due to spin dependent scattering generated by spin-orbit coupling, spin up electrons are preferentially scattered in direction parallel to *y*-axis while spin down electrons are preferentially scattered in the opposite direction. Since $n_{\uparrow} = n_{\downarrow}$, there is not a net transport of electrons along *y*, but there is a net pure spin current density (that is a spin transport with no charge transport associated) along that direction, generated by an unpolarized current in the transverse direction (charge to spin conversion). This spin current generates a spin accumulation at the edges of the slab [14]. This effect is called spin-Hall effect (SHE).

The inverse of this effect, called inverse spin-Hall effect (ISHE), is shown in Fig. 2.6 (b). Again, we have a flux of electrons flowing in the *x*-direction, but now there is an imbalance between the electrons with spin parallel and anti-parallel, with respect to the *z*-axis. Therefore, the current is spin polarized with a polarization $\boldsymbol{P}$ defined as in Eq. (2.1.1) and we can define a spin density current as in Eq. (2.2.3). Due to the asymmetry in scattering, electrons with opposite spin polarization are deflected in opposite directions along the *y* axis. Since the number of spin-up and spin-down electrons is different, there will be a larger number of electrons scattered in one direction than in the other, creating a net flux of electrons moving in *y*-

direction. Therefore, ISHE transforms a spin-polarized current into an electric current (spin-to-charge conversion).

The expression for the charge current density generated by ISHE can be expressed as follow [21,22]:

$$\boldsymbol{J}_c = \gamma \boldsymbol{J}_s \times \boldsymbol{u}_s, \tag{2.2.4}$$

where $\boldsymbol{J}_s$ is the spin current density, $\boldsymbol{u}_s$ is a unit vector parallel to the spin polarization, γ is the spin-Hall angle, a dimensionless parameter proportional to the spin-orbit strength, which provides for the efficiency of the spin-to-charge conversion. Given the conductivity of the slab σ, the electromotive field generated by ISHE is, using Eq. (2.2.3):

$$\boldsymbol{E}_{ISHE} = \gamma/\sigma \boldsymbol{J}_s \times \boldsymbol{u}_s = D_{ISHE} \boldsymbol{J}_s \times \boldsymbol{u}_s. \tag{2.2.5}$$

Besides its possible application in the field of spintronics, ISHE can be exploited to measure spin currents. Indeed, in materials with high spin-orbit coupling, so with high γ, the spin current density $\boldsymbol{J}_s$ is converted into a detectable current density $\boldsymbol{J}_c$, through which we can indirectly infer information about $\boldsymbol{J}_s$. If the spin current is generated in a material where γ is not sufficiently high to provide for an efficient detection, ISHE detection can be performed transferring the spin population to a second material with high spin-orbit coupling, which works as an ISHE detector. Having said that, ISHE offers a technique to study optical orientation in semiconductors. K. Ando in 2010 exploited this technique in the case of GaAs and showed how to combine ISHE and optical orientation to convert light polarization information into an electric signal [9]. The same results have been achieved using Ge [10-13,32].

The device used for the measurements is shown in Fig. 2.7 in the case of Ge/Pt heterostructure. A thin film of Pt (few nanometers) is grown on top of the semiconductor, where Pt, thanks to its large atomic number, is a suitable material as ISHE detector. A spin density s is generated into the semiconductor using circularly polarized light and generates a spin current density. In open circuit condition, $\boldsymbol{E} = 0$ and the spin current density is driven only by diffusion, so $\boldsymbol{J}_s \propto -\boldsymbol{\nabla} s$. Since the Pt layer is non-magnetic, $s = 0$ in it and spin majority electrons, driven by the gradient, diffuses by thermionic emission through the Schottky barrier from Ge to the Pt layer. The spin current density $\boldsymbol{J}_s$ injected into the Pt layer is then is parallel to z while $\boldsymbol{u}_s$ is parallel (or antiparallel) to the wave vector $\boldsymbol{k}_{opt}$. In Pt layer, ISHE converts $\boldsymbol{J}_s$ into an electromotive field as shown in Eq. (2.2.5). When the measurement is performed in open circuit condition, the electromotive force associated to $\boldsymbol{E}_{ISHE}$ is balanced by an opposite voltage, ΔV_{ISHE}, which is measured

by two gold electrodes. It is important to notice that, given the geometry of Fig. 2.7, since $\boldsymbol{J}_s$ is parallel to z, in order to generate ISHE in the Pt

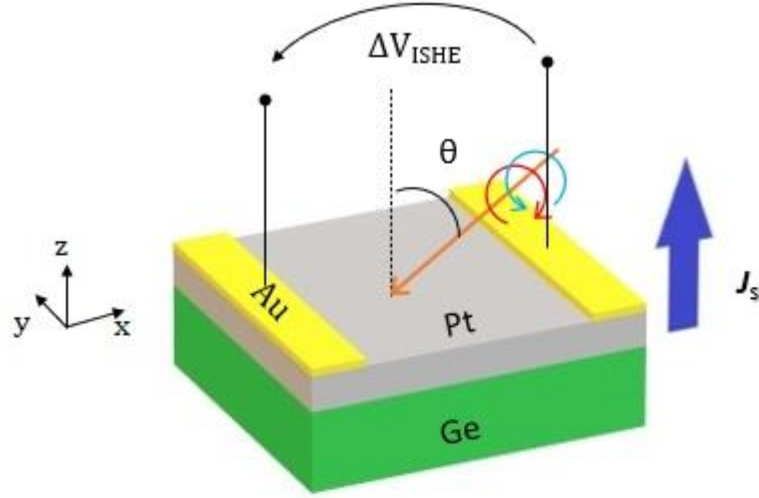

Fig. 2.7 *Schematic representation of Ge/Pt heterostructure used for photoinduced ISHE.*

layer, the spin polarization must have an in-plane component. This can be achieved impinging with the light beam at grazing incidence. In Fig. 2.7, the voltage drop ΔV_{ISHE} measured between the two Au electrodes is generated by the x-component of the ISHE electromotive force:

$$\Delta V_{ISHE} \propto |\boldsymbol{J}_s \times \boldsymbol{u}_s|_x = J_s \sin\vartheta \cos\varphi, \qquad (2.2.6)$$

where θ and φ are the polar and the azimuthal angle of the incoming wave vector. It should be notice that, due to refraction, the light beam is absorbed in Ge with a polar angle θ_{Ge} which is different from θ. Since the optical orientation takes place in Ge, the spin polarization is then oriented according to θ_{Ge} and is this angle that should enter in Eq. (2.2.6). However, the dependence on θ enters in the equation through the Snell law, since $\sin\theta_{Ge} = \frac{1}{n_{Ge}}\sin\theta$, where n_{Ge} is the refractive index of Ge.

Using Eq. (2.2.2) and Eq. (2.2.3), we can see that J_s depends on the on the density of photogenerated electrons n, which depends on the intensity of the light beam I_{in}, and on its spin polarization P. Since the spin polarization of the photogenerated electrons depends on the photon energy, as shown in section 2.1.3, the photon energy will also enter in the equation for ΔV_{ISHE}. However, the values of P shown in Fig. 2.6 (b) for the case of Ge, are obtained in the case of a fully CPL. In the

general case of an elliptically polarized light, *P* must be corrected by the degree of circular polarization (*DCP*) of the light beam, defined as;

$$P_{circ}^{air} = \frac{I_R - I_L}{I_R + I_L} = \frac{2A}{1+A^2}, \qquad (2.2.7)$$

where I_R and I_L are the intensities of the RCP and LCP light, respectively and *A* is the ellipticity of the light beam, defined as the ratio of the minor to major radiuses of the elliptically polarized light. *A* takes values from 0, for linearly polarized light, to 1, for CPL. If we include these factors in Eq. (2.2.6), we obtain:

$$\Delta V_{ISHE} \propto P(hv) P_{circ}^{air} \, I_{in} \sin\vartheta \cos\varphi. \qquad (2.2.8)$$

We can see that we have no signal in the case of linear polarization, while the signal is maximum (in absolute value) if we used a fully circularly polarized light. Moreover, since $P_{circ}^{air} = \pm 1$ for RCP (LCP), ΔV_{ISHE} switches sign as we move from RCP to LCP, coherently with the fact that photons with opposite circular polarization generates a spin polarization oriented in opposite directions. This feature allows to perform a differential detection whit the possibility of improving the signal to noise ratio (See Chapter 5).

Again, it should be notice that in Eq. (2.2.8) we have referred to the DCP and intensity of the illuminating light while, for the purpose of optical orientation, we should have used the DCP and the intensity of the light absorbed by the semiconductor. But when the light passes through layers with different refractive indexes at grazing incidence, it changes not only its intensity but also the ellipticity. In general, we have that $I_t^{Ge} \neq I_{in}$ and $P_{circ}^{Ge} \neq P_{circ}^{air}$ where I_t^{Ge} and P_{circ}^{Ge} are the intensity and the DCP of the light transmitted to Ge. Under the assumption that the imaginary part of the complex index n_{Ge} for Ge and the transmission coefficient $t^{s(p)} = E_t^{s(p)} / E_i^{s(p)}$ for the Ge/Pt hybrid heterostructure (where $E_t^{s(p)}$ and $E_i^{s(p)}$are the transmitted and incident electric field amplitudes for *s* (*p*)-polarized plane wave) are negligibly small, we can write that [38]:

$$A_{Ge} = A \frac{t^s}{t^p}, \qquad (2.2.9a)$$

$$P_{circ}^{Ge} = \frac{2 t^s t^p A}{(t^p)^2 + (t^s)^2 A^2}, \qquad (2.2.9b)$$

$$I_t^{Ge} = \left[(t^s)^2 \frac{A^2}{1+A^2} + (t^p)^2 \frac{1}{1+A^2} \right] n_{Ge} \cot\theta_{Ge} \, \tan\theta \, I_{in}. \qquad (2.2.9c)$$

If now we substitute P_{dcp} and I_{in} in Eq. (2.2.8) with Eq. (2.2.9b) and Eq. (2.2.9c), we find that:

$$\Delta V_{ISHE} \propto P(h\upsilon) \cos\varphi \, t^s t^p \cos\theta_{Ge} \, \tan\theta \; P_{circ}^{Ge} \, I_{in}. \qquad (2.2.10)$$

As can be seen in Eq. (2.2.10), the linear dependence of the ISHE signal from the DCP and the intensity of the irradiating light is preserved, although the dependence on the polar angle θ is trickier.

Thanks to the linear dependence of the ISHE signal form the degree of circular polarization, the device enables the conversion of light-polarization information into an electric information, as suggested by K. Ando [9], where a RCP ($P_{circ} = 1$) light generates a high volage state, while a linearly polarized light ($P_{circ} = 0$) a zero voltage state.

Chapter 3
Graphene/Ge sample: design and fabrication

The following chapter introduces the design and the fabrication processes of the sample used to measure the diffusion of optically generated spin currents in graphene. To overcome the problem of small spin-orbit coupling in graphene, we realized a graphene/Ge Schottky junction, where the spin current is optically generated in Ge through optical orientation and then eventually diffuses in the graphene overlayer. After the diffusion in the graphene layer, the spin current reaches a thin Pt pad, used as ISHE detector, where it is converted into a voltage drop.

The Schottky diode and the ISHE detector have been fabricated using electron beam lithography (EBL) performed at the L-Ness laboratories of Politecnico di Milano in Como, in collaboration with the Nanoscale Device group.

3.1 Sample design

Fig. 3.1 shows the layout of the sample used for the measurements. We evaporated a 100 nm thick SiO_2 insulating layer on top of $< 001 >$ slightly n-doped ($N_D \approx 10^{16} cm^{-3}$) bulk Ge substrate. Then, we etched the SiO_2 opening a $200 \mu m \times 200 \mu m$ window such that, when we transfer graphene on top of the structure, we from a graphene/Ge Schottky junction in that area (the blue square in Fig. 3.1 (a)). A 4 nm thick Pt pad was evaporated on top of graphene, in a region where the thick oxide layer separates graphene from Ge. The position of Pt with respect to the graphene/Ge Schottky junction is characterized by a distance d_{Pt-Ge}, as can be seen

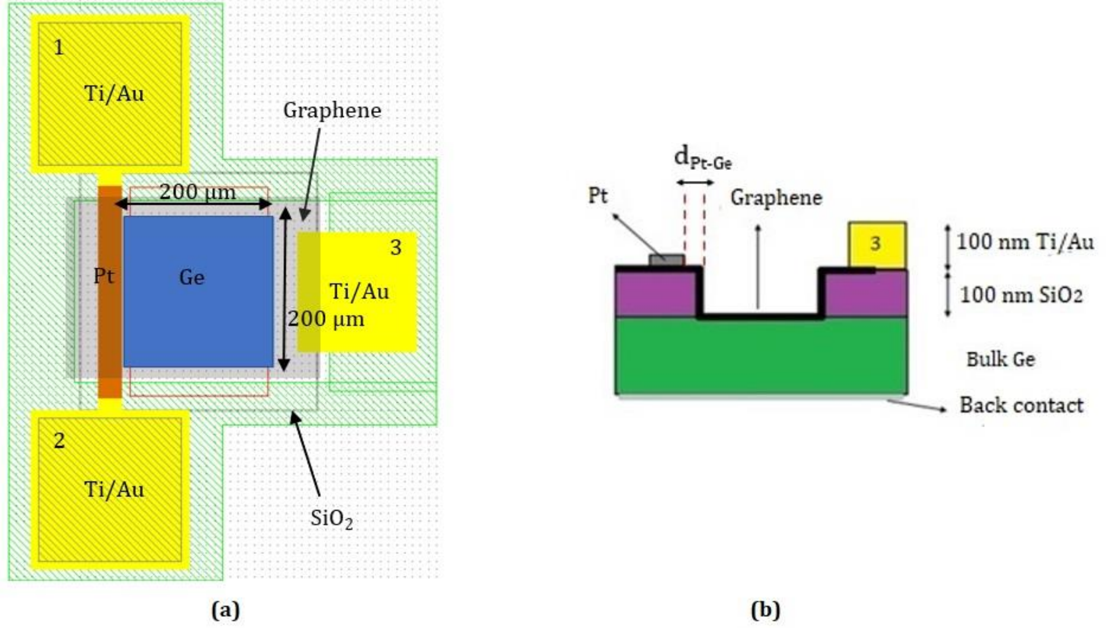

***Fig. 3.1** Top view **(a)** and vertical section **(b)** of the detector layout.*

in Fig. 3.1 (b). On top of the oxide layer, we deposited three 100nm thick Au pads on top of a 2nm layer of Ti. Two of them are in contact with the Pt pad (Au pad 1 and 2 in Fig. 3.1) and one pad electrically connects the graphene sheet (pad 3 in Fig. 3.1). Finally, we evaporated a thin AgSb alloy on the back of the structure, which forms an ohmic contact with Ge. The graphene/Ge junction can be biased by applying an electrical voltage between pad 3 and the back contact (see Chapter 4). In order to test spin injection and spin transport in graphene, we focused a circularly polarized light on the graphene/Ge Schottky junction area. Since graphene is almost transparent in visible and NIR range, with an absorption $\alpha \approx 2.3\%$ per layer [40], the light is almost entirely absorbed in Ge, generating a spin polarized electron population in the conduction band of Ge with a spin density $s = n_\uparrow - n_\downarrow$, as described in Chapter 2.1. These spin polarized electrons eventually diffuse in graphene, driven by the large spin density gradient at the Ge/graphene interface ($s = 0$ in graphene, since we do not generate polarization there). To measure the spin current transported by graphene, we exploited ISHE in the Pt pad, which works as an ISHE detector. The spin current indeed diffuses in graphene until it reaches the Pt pad, where it is converted into a voltage drop, measured between the gold pad 1 and 2. As can be seen in Fig. 3.1, the ISHE detector is separated from the Ge substrate by the insulating oxide layer, and the only connection between the Pt pad and the region where we generate the spin current is graphene. Thanks to this

design, the spin current cannot directly flow from Ge to the Pt pad, and we are able to measure only the spin current transported by graphene.

On a single chip, we have fabricated 46 structures like the one shown in Fig. 3.1, changing the position of the Pt pad with the parameter d_{Pt-Ge} taking values of 1μm, 2μm, 5μm, 10μm and 20μm. The purpose of this choice is to change the length over which the spin current diffuses in graphene before reaching the Pt detector, which would allow us to study the spin diffusion in graphene. Moreover, we have also fabricated 3 test structures with Pt directly grown on top of Ge and no graphene layer. In this way, we also have conventional Ge/Pt Schottky junction we can rely on for both the electrical characterization of the structures and the ISHE measurement. All these structures are arranged in 7x7 matrix, according to Fig. 3.2.

7.7

A	B	C	D	E	F	AS
AS	BS	CS	DS	ES	BS	CS
C	CS	D	AS	C	A	B
BS	ES	F	CS	BS	CS	AS
DS	BS	AS	E	B	A	BS
F	CS	B	A	BS	DS	A
B	AS	C	ES	D	E	C

1.1

(a)

	Ge Pt distance
A	1um
AS	
B	2um
BS	
C	5um
CS	
D	10um
DS	
E	20um
ES	
F	Test

(b)

Fig.3.2 ***(a)*** *Positions of different types of structures in the 7x7 matrix and* ***(b)*** *corresponding values of Pt-Ge distance.*

3.2 Sample fabrication

The structures described above was fabricated on a $1.5cm \times 1.5cm$ substrate of crystalline Ge, covered by a 100 nm thick layer of SiO_2, fabricated at the Polifab facility of Politecnico di Milano. The first step is to remove the SiO_2 in the regions where we are going to form the graphene/Ge Schottky junctions. A layer of positive PMMA resist is spin coated on top of the sample and baked for 5 minutes at 160 °C to dry the solvent. The areas where we want to remove the oxide were exposed to an electron beam accelerated by a 10kV potential, using the Raith E-Line system of the Nanoscale Device Group at L-Ness. The electron beam exposure alters the nature of the resist, by breaking the chemical bonds, with the result that a subsequent immersion of the sample in a developer solution removes the exposed parts of the resists. The exposed resist is removed by merging the sample in 1:3

MIBK: Isopropanol solution for 1:30 minutes, which works as developer, followed by a rinsing for 1 minute in isopropanol, which works as stopper. The oxide is then etched using a buffered oxide etch (BOE), obtained by a solution 1:6 of NH_4F and HF for 2min:45sec. The BOE etches the SiO_2 in the regions that were exposed to the electron beam, while in the other areas the resist protects the sample. The sample was then washed in deionized water and left in acetone for about 4-5 hours, in orders to remove the unexposed resist. Finally, the sample was rinsed in isopropanol and dried with a nitrogen flux. At the end of this process, we have opened forty-six $200\mu m \times 200\mu m$ squared windows and three $200\mu m \times 600\mu m$ rectangular windows in the oxide layer. The former corresponds to the positions where we allocated the Graphene/Ge Schottky diodes and the latter to the positions of the test structures, according to Fig. 3.2. Fig. 3.3 shows the result of the etching for a standard and a test structure. Before proceeding to the next step, the graphene transfer, we deposited the back contact (AgSb) on the back of the sample by e-beam evaporation.

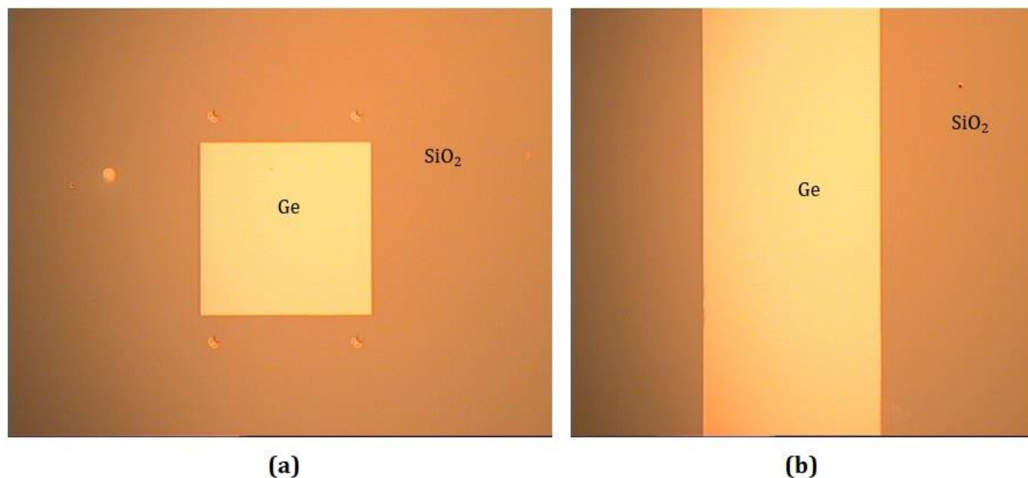

Fig. 3.3 *Standard structure **(a)** and test structure **(b)** after the etching of the SiO_2 layer.*

3.2.1 Graphene wet transfer

We used a CVD graphene grown on a Cu substrate, produced by Graphenea®. The problem of using CVD-graphene grown by catalytic action of a metallic substrate at high temperatures is the that we need to get rid of the metallic substrate when we want to implement graphene on device. We used a PMMA-mediated wet approach, where a spin-coated PMMA layer is used as an intermediated substrate to transfer graphene from the Cu substrate to the device.

We started cutting a small piece of the Cu foil and fixed it with adhesive tape to a wafer and we spin coated a layer of PMMA on top of it (Fig. 3.4(b)). Since the Cu substrate was covered on both the sides, we used the graphene on the side covered with PMMA while we needed to remove the graphene on the other side. In this sense, the adhesive tape has a double function: it fixes the piece of Cu on the wafer during the spin coating of PMMA and it prevents the polymer to go beneath the bottom side of the foil, depositing on the graphene sheet that we want to get rid of. In that case, the PMMA not only would protect the unwanted graphene layer but also protects the Cu from etching.

After the PMMA was spin coated and heated for 5 minutes at 160 °C, we flipped the foil, and we removed the back graphene using an O_2 plasma etching in a Tepla plasma asher machine. At this point we have a PMMA/graphene/Cu stack (Fig. 3.4(c)) and we are ready to etch the Cu. We first immerged the stack into a 5:1:1 solution of deionized-H_2O:H_2O_2:HCl for about one minute, which removed most of the Cu substrate, and then we soaked it in a solution 2:1 of H_2O:$FeCl_3$ for a about 3~4 hours to remove all the Cu.

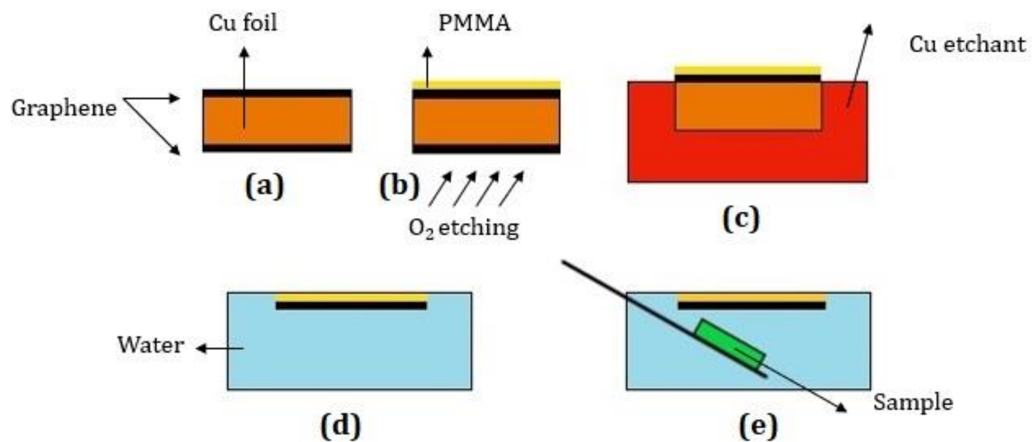

Fig. 3.4 *Main steps of graphene wet transfer:* ***(a)*** *graphene is CVD grown on top and bottom of a Cu foil.* ***(b)*** *PMMA is spin coated on top of the foil and back graphene is removed with oxygen plasma etching.* ***(c)*** *Cu is etched in acid solution while PMMA gives the support for graphene.* ***(d)*** *The PMMA/graphene stack is rinsed in deionized water.* ***(d)*** *Fishing with the sample.*

In between of these two operations, the foil was rinsed in deionized water in orders to wash away the acid residues from the first etching.

At this point, the Cu substrate was completely etched and the graphene remained sticked to the PMMA layer (Fig. 3.4(d)). We rinsed the PMMA/graphene foil in different basins of deionized water again to remove the residuals of copper etchant. To move the sample from one basin to the other, we used a glass slide, fishing the sample from the water. During this operation, it is important to avoid the formation of bubbles beneath the graphene: bubbles must remain on the slide. Indeed, if some bubbles form beneath graphene, they will explode when we heat the sample, breaking the graphene layer.

The transfer of the PMMA/graphene layer to the sample is shown in Fig. 3.4(e). We glued the sample to a slide, and we fished the PMMA/graphene from deionized water placing the sample beneath the graphene layer. In this way, graphene adheres to the sample's surface, while the PMMA support remains on top. During this operation, we must take care that graphene should cover all the surface of the sample without wrinkling around the edges of the slide. We than left the slide inclined to drain for the night and then baked the sample for 5 minutes at 150 °C, in orders to soften PMMA and promote graphene adhesion on the sample. The last step is to remove the PMMA support, soaking the sample into acetone and then rinsing it in isopropanol, as described above.

3.2.2 Graphene etching

We want to create a graphene-free region in each structure, which can be seen in Fig. 3.1(a) as the green T-shaped region, and we also need to remove graphene from the test structures.

To etch graphene, we used a reactive ion etch (RIE) O_2 plasma. The basis of plasma assisted etching is to use a gas flow discharge to deionize an otherwise relatively stable molecules, generating chemically reactive species which react with the solid to be etched to form volatile products [38]. Since no chemical solution is used during the etching, RIE is considered a dry etching technique.

In this case, we used a low-pressure oxygen plasma. Indeed, when O_2 is ionized, it forms O^+ ions which react with the carbon atoms of graphene. The scheme of a vacuum chamber for RIE is shown in Fig. 3.5. We have two conductive plates with the sample lying on the bottom one. The top plate and the walls of the chamber are grounded, while the bottom plate is coupled by a capacitance to a RF source. A system of rotary and turbo pumps creates vacuum in the chamber. When the pressure reaches 30mTorr, we starte injecting a controlled O_2 flow into the chamber. A strong radiofrequency (13.56 MHz) excitation is applied between the two plates, stripping electrons from the oxygen molecules. These electrons are then accelerated by the radiofrequency and collide with other molecules, creating more

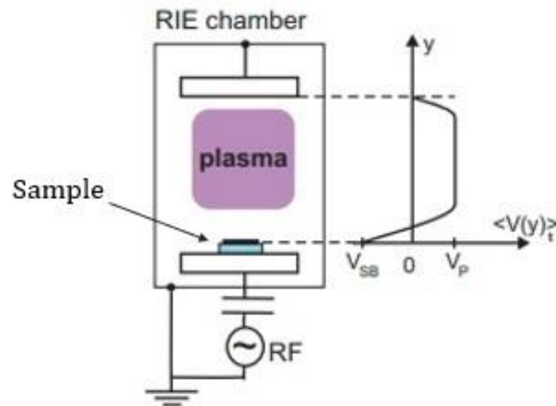

Fig. 3.5 *RIE chamber scheme. The sample is placed on the bottom plate, which is coupled by a capacitance to a RF source. Due to the positive potential of plasma and the negative potential on the bottom plate, ions are accelerated toward the bottom plate, where they react with the sample. Figure adapted from [39].*

electrons and more ions. This avalanche process leads then to the formation of a plasma. In each cycle, electrons can hit the top plate or the walls of the chamber. In this case, they are fed out to ground. Instead, if electrons are absorbed by the bottom plate, due to the DC isolation (see Fig. 3.5), they build up a negative potential there. The more massive ions move relatively little in response to the RF field, and so the plasma acquires a net positive charge. Combining this effect with negative charging of the bottom plate, oxygen ions are accelerated toward the bottom plate, where they eventually react with C atoms etching the graphene. Thanks to the high anisotropy and selectivity that RIE can provide, it is possible to obtain well defined and etched areas.

We first prepared the sample for the EBL covering it with three layers of PMMA for etching. Each layer was spin coated at 6500 rpm for 30 seconds, and then baked at 160 °C for 5 minutes. With the EBL, we exposed the areas where we wanted to remove graphene, and then we removed the exposed PMMA as explained before. Fig. 3.6 shows the optical images for the graphene/Ge Schottky diode structures and the test structure obtained after the EBL explosion and after the development of the exposed resist. In the brighter areas, the PMMA still covers the structures, while it was removed in the darker regions. Therefore, during RIE, graphene is removed from these regions, while the PMMA protects it where necessary. The PMMA also covers Ge (the orange square) in the standard structures, which indeed will preserve the graphene/Ge Schottky junction. Instead, in the test structure, the

PMMA was removed from Ge and there will be no graphene on top of it after the plasma etching.

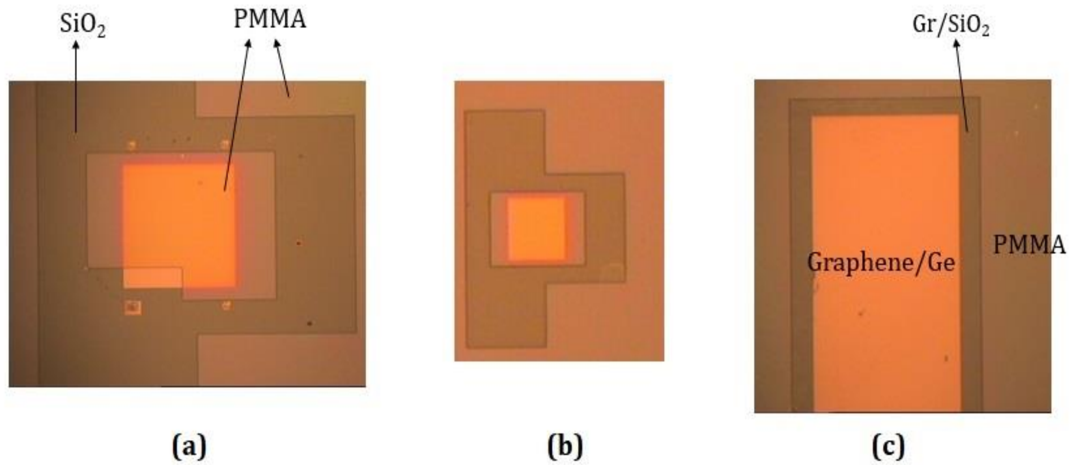

Fig. 3.6 *Structures 1.2 (**a**), 2.5 (**b**) and the test structure 2.1 (**c**).*

The last step is to remove the remaining PMMA, soaking the sample in acetone, as explained before. Results are shown in Fig. 3.7. The optical images have been taken in dark field mode to better appreciate the presence of graphene. As can be seen, graphene has been etched from the region that were exposed during the EBL, while it is present all around.

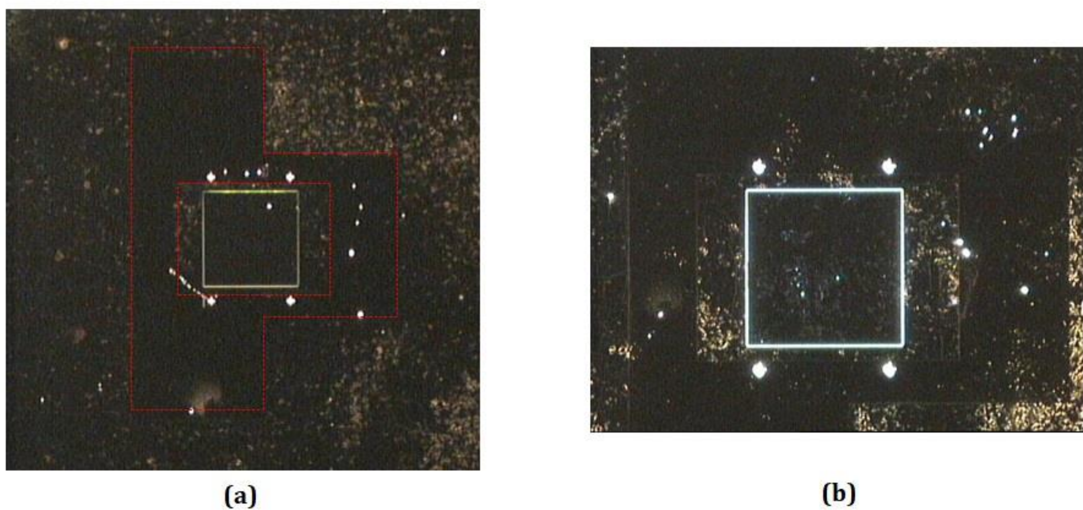

Fig. 3.7 *Optical images taken in dark field mode of the structures after the graphene etching process is terminated. In dark filed microscopy, only the light scattered by the*

*sample is focus on the detector. Dark field microscopy allows to image also transparent objects. (**a**) Structure 1.1. (**b**) Structure 7.3.*

3.2.3 Pt detector and Ti/Au contacts deposition

The last two steps are the fabrication of Pt detectors and of the Ti/Au contacts. For the depositions of the metals, we have electrons beam evaporation. An e-beam is generated by heating a tungsten filament and it is focused on a crucible, filled by the metal that we want to deposite. As electrons hit the metal, they lose their kinetic energy evaporating the metal, which is deposited on the sample, placed upside down above the crucible. A homogeneous deposition can be obtained using low pressure ($< 10^{-6}$mbar) and low deposition rate, controlled by the power the crucible is heated with. The deposition rate is controlled by a quartz crystal microbalance, whose oscillating frequency depends on the mass per unit area deposited on top of it. The unwanted metal is then removed by a lift-off process. To perform the lift-off, a mask is created on the surface of the sample, before the deposition of the metal. The mask is created using EBL, where we exposed the areas where we wanted to have the metal structures. After the evaporation, the sample was soaked into acetone for a couple of hours. Some scratches were done on the surface of the sample to promote the penetration of the acetone. Acetone removes the unexposed PMMA and the metal on top of it and, at the end of the process, the metal is left only in the areas where the PMMA was removed after the exposure.

To enhance the lift-off process, we deposited two different layers of PMMA, one with high molecular density on top of one with low molecular density. In this way, since the low weight PMMA is more sensitive than the high weight PMMA, when we develop the resist in the MIBK:isopropanole solution, the resist develops an enhanced under-cut. This process is summarized in Fig. 3.8.

For the ISHE detectors, we deposited a 4nm thick layer of platinum. The Pt detectors are placed at different distances from the edge of the Ge window (Fig. 3.10), as explained in section 3.1. In Fig. 3.9 it is reported the optical image one of the test structure after the development of the resist and before the deposition of Pt. The Pt detector is deposited in the small rectangle in the middle.

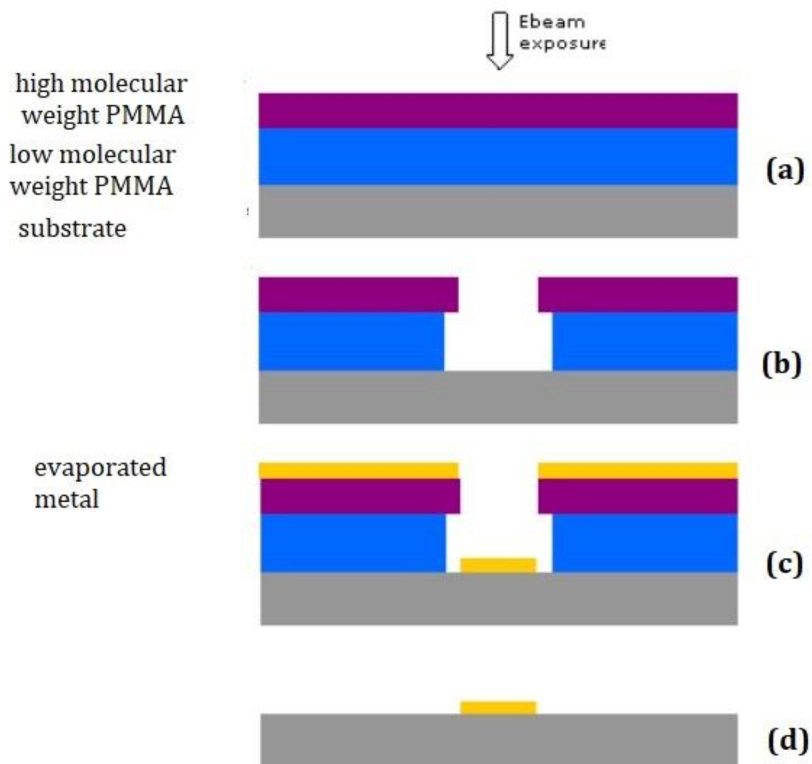

Fig. 3.8 *Lift off process with a PMMA bi-layer. (**a**) A high weight PMMA is spin-coated on top of a low weight PMMA and exposed to the electron beam. (**b**) PMMA is developed in a mixture of MIBK and IPA and the exposed layers of PMMA are removed, forming an enhanced undercut. (**c**) Metal deposition. (**d**) Thanks to the presence of the undercuts, acetone removes the remaining PMMA with the metal on top. The metal remains only in the regions that were exposed.*

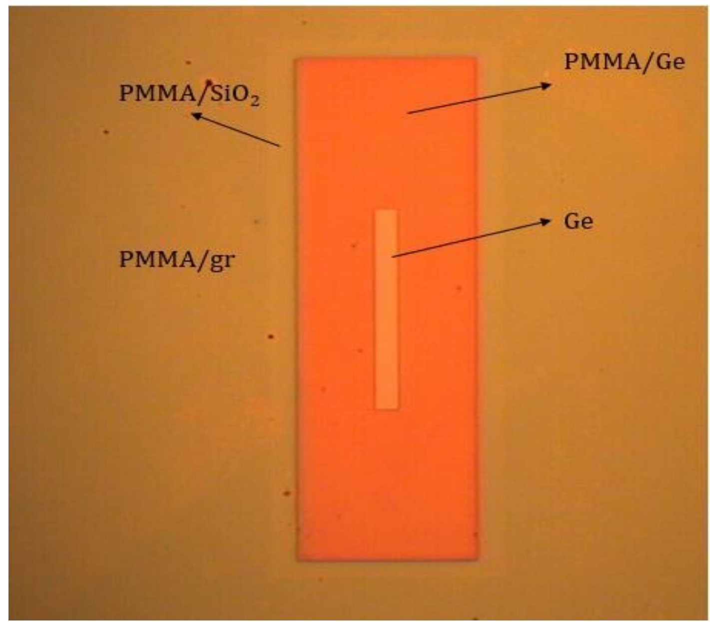

Fig. 3.9 *Test structure 2.1 after the resist development, before the Pt deposition.*

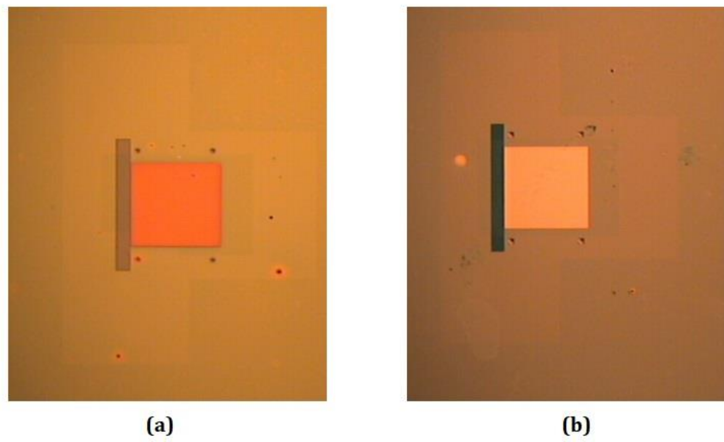

Fig. 3.10 (a) *Structure 1.2 after resist development, before Pt deposition.* ***(b)*** *Structure 1.2 after Pt deposition and lift-off.*

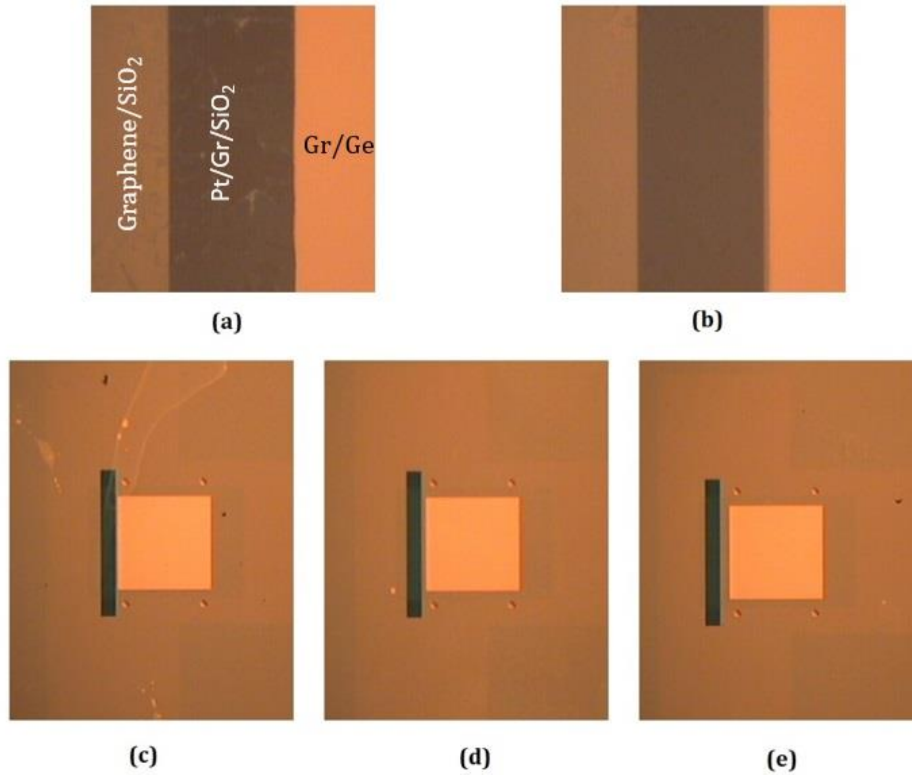

Fig. 3.10 *Pt stripes for the five different type of structures, with different distance between Ge and Pt. (**a**) Structure 7.7, 1µm. (**b**) Structure 6.2, 2 µm. (**c**) Structure 5.5, 5 µm. (**d**) Structure 3.1, 10 µm. (**e**) Structure 4.2, 20 µm.*

For the deposition of the Au contacts, the evaporation was performed at 10^{-7}mbar. We first evaporated 2 nm of Ti with a rate of $0.5\ \text{Å}/s$, followed by the evaporation of 100 nm of Au performed at a rate of $0.5\ \text{Å}/s$ up to 15 nm. The growing rate was then brought to $1\ \text{Å}/s$ with a rising time of one minute and a linear slope. The final result, after the lift-off, is shown in Fig. 3.11.

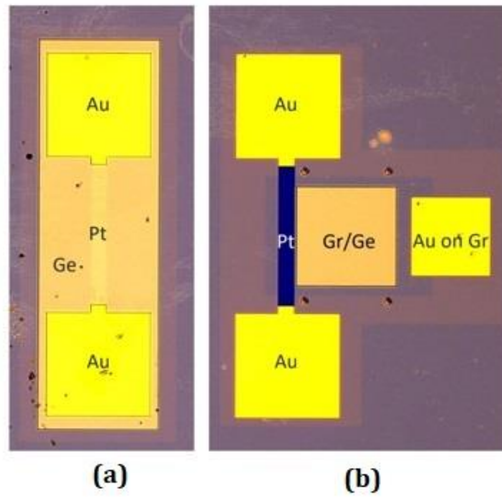

***Fig. 3.11** Optical images of the final test **(a)** and standard structures **(b)**.*

Chapter 4
Electro-optical characterization

The following chapter presents the results of the electrical and optical characterization of the graphene/Ge device, with the aim of testing the formation and the quality of the graphene/Ge Schottky junction. The electric measurements have also been used to extrapolate the main parameters of the Schottky junction, such as the Schottky barrier height φ_b, the ideality index n and the Richardson constant for Ge (001) A^*. For this purpose, we have first measured the I-V characteristics of the structures at room temperature and then we investigated this behaviour for different temperatures.

In the optical characterization, we investigated the behaviour of the structures as photodetectors. A measurement of the photocurrent as a function of the incoming power should resemble the typical characteristic of graphene/semiconductor Schottky junctions shown in Chapter 1.3.

The electrical characterizations both at room temperature and as a function of the temperature was performed at the L-Ness laboratories in Como, under the supervision of prof. G. Isella and Dr. L. Anzi from the Nanoscale device group, while the optical characterization was performed at the SemiSpin Lab of Politecnico di Milano, under the supervision of Dr. F. Bottegoni and Dr. C. Zucchetti.

4.1 I-V characterization

To measure the I-V curve of the graphene/Ge Schottky junction, we biased the junction applying an electric voltage between the back contact and the pad 3, as shown in Fig. 4.1 (a), and we measured the current intensity flowing. The sample lied on a grounded metallic plate which grounded the germanium substrate through

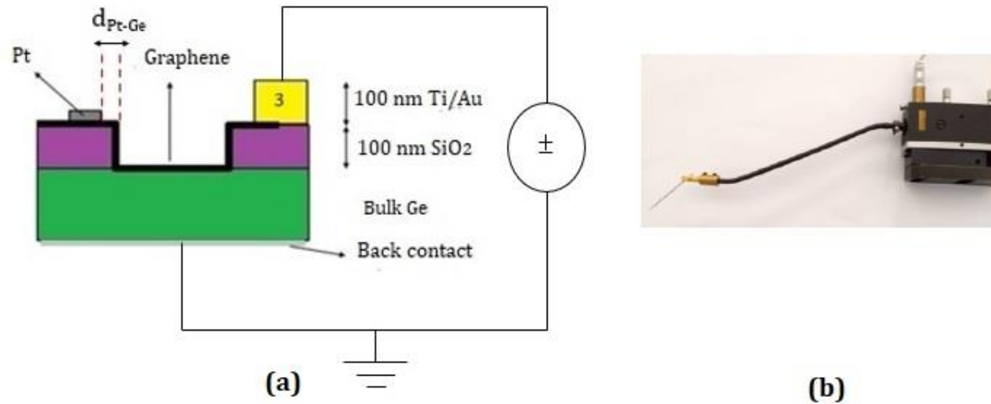

Fig. 4.1 ***(a)*** *Scheme of the electrical connection for the I-V characteristic measurement.* ***(b)*** *Picture of the probe used to connect the Au pad.*

the back contact. The electric voltage on pad 3 was applied by means of a probe as the one in Fig. 4.1 (b) connected to a Keithley source-meter, which also measures the current intensity *I*. Since pad 3 is electrically connected to graphene, we applied a voltage to graphene side of the Schottky junction. The Schottky junction is forward biased when we apply a positive voltage on the pad 3, while the reverse bias is obtained by applying a negative voltage on the pad, as explained in Section 1.2. We measured *I* for an applied voltage ranging from -3V to 1V, with a sensitivity $\Delta V = 2$ mV.

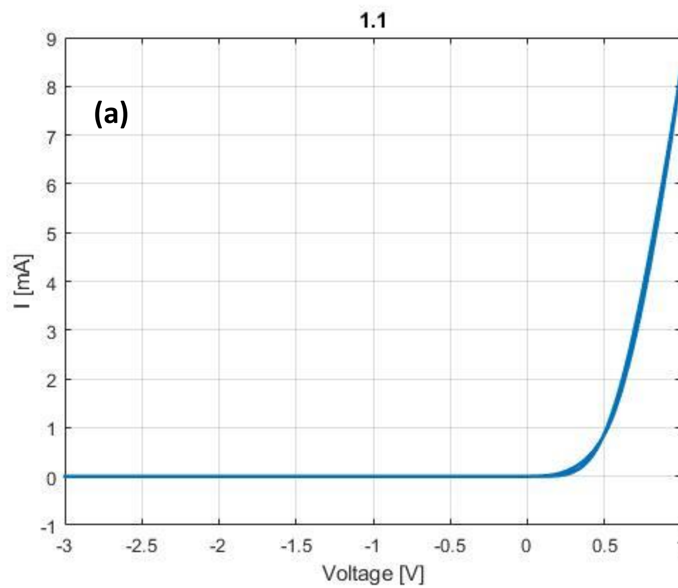

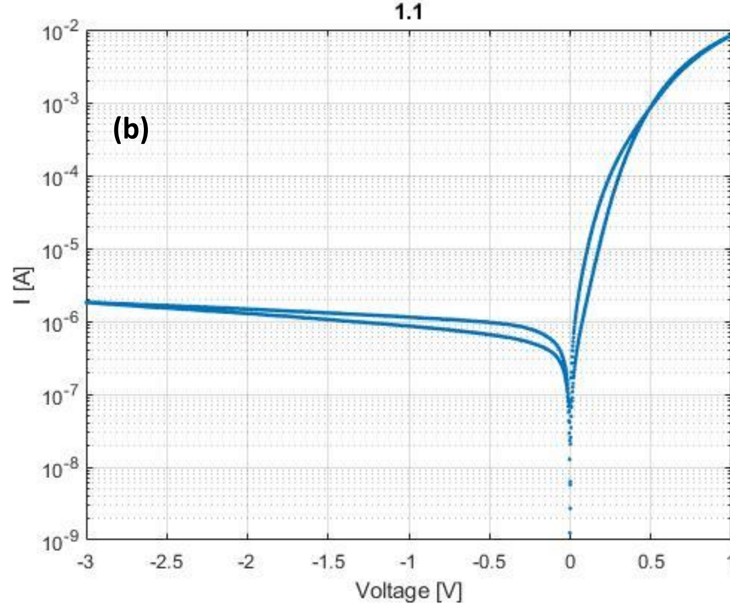

Fig. 4.2 *Forward and reverse bias current-voltage characteristic in linear* ***(a)*** *and semi-logarithmic* ***(b)*** *scale.*

Fig. 4.2 shows the current-voltage characteristics in linear and logarithmic scale. The rectifying behaviour is in good agreement with the thermionic emission theory, as expected from a Schottky junction where a low n-doped semiconductor is involved, although at high forward voltage there is a deviation from exponential to linear behaviour. To explain this effect, we need to take into account the series resistance R_s. The series resistance depends on several factors, such as the semiconductor resistivity, the contact resistance, the resistance between the probe and the metal pad and from others geometrical factors [5]. All these effects are represented by a resistance put in series to the Schottky diode, as shown in Fig. 4.3. The effect of the series resistance is that, when we apply a bias V, the effective voltage that drops across the Schottky junction is:

$$V_{eff} = V - R_s I. \tag{4.1.1}$$

Therefore, the correct equation describing the current-voltage characteristic for a Schottky junction is, using thermionic emission:

$$I = I_s\left(e^{qV_{eff}/nk_bT} - 1\right),\ I_s = AA^* e^{-\varphi_b/k_bT}, \tag{4.1.2}$$

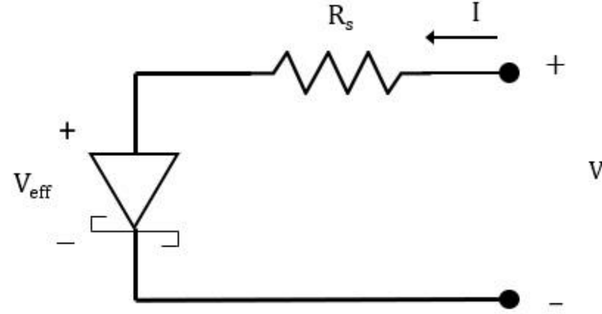

Fig. 4.3 *Equivalent circuit for the graphene/Ge Schottky diode, taking into account the series resistance. Figure adapted from [5].*

where A is the area of the Schottky junction. When we apply a reverse bias, the Schottky diode is in off state, and the current intensity that can flow in the circuit is limited to I_s as can be seen in Fig. 4.2. The small voltage dependence of I_s can be related to the bias dependent Schottky barrier in graphene/semiconductor Schottky junction, as explained in Chapter 1, and to other leakage effects, which can be schematized by adding a shunt resistance in parallel to the Schottky diode. When we apply a positive voltage V, the Schottky diode is forward-biased and the current intensity starts to increase exponentially. But, as I grows, the voltage drop on the series resistance $R_S I$ also increases, reducing the effective voltage applied on the Schottky junction, while the current flowing into the circuit is now driven by the series resistance, giving the linear behaviour of Fig. 4.2.

R_s is calculated by a linear fit of the data in the range of large forward bias. For the structure 1.1, the interpolation between 0.9V and 1V gives $R_s = 48.5\Omega$, calculated as the inverse of the slope of the red line in Fig. 4.4. Once we have R_s, we can calculate V_{eff} as in Eq. (4.1.1). The actual *I-V* curve for the Schottky junction is obtained by plotting I vs V_{eff}, as shown in Fig. 4.5 in semilog-scale. The linear behaviour observed in forward mode proves the exponential rectifying behaviour, as predicted from the thermionic emission.

The experimental values of the barrier height φ_b and the ideality index n were extrapolated from the data by a linear fit of $\ln(I)$ vs V_{eff}. Using Eq. (4.1.2) in the limit $qV_{eff} \gg nk_bT$, we can write:

$$\ln(I) = ln(I_s) + \frac{q}{nk_bT} V_{eff}. \quad (4.1.3)$$

From the slope and the intercept, we can retrieve n and I_s respectively, while φ_b is calculated from I_s as:

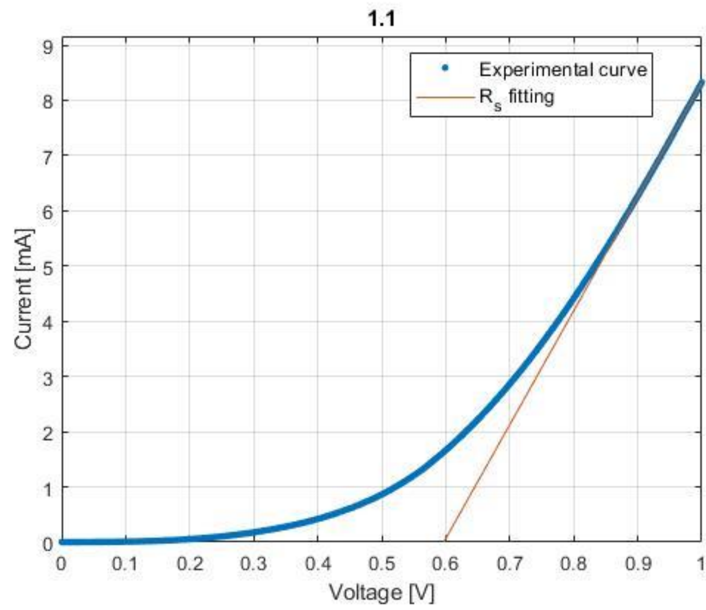

Fig. 4.4 *Linear fit performed to extrapolate the series resistance from the I-V characteristic for the structure 1.1. The linear fitting is performed between 0.9V and 1V.*

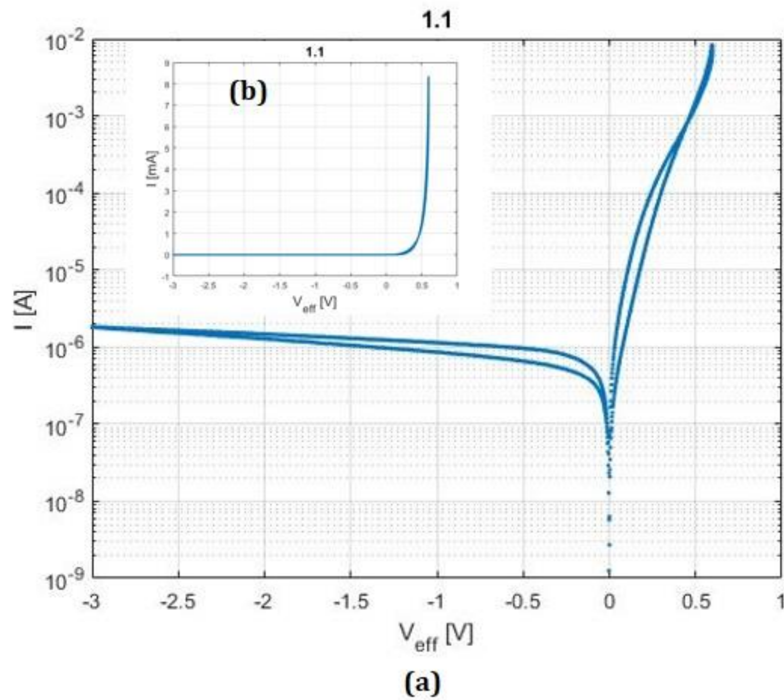

Fig. 4.5 ***(a)*** *Semilogarithmic plot of current vs the effective voltage V_{eff} that drops on the junction, for the structure 1.1. The inset* ***(b)*** *shows the same characteristic in linear scale.*

$$\varphi_b = k_b T \ln\left(\frac{AA^* T^2}{I_s}\right). \tag{4.1.4}$$

The linear fit is performed in the bias range $0.08V < V_{eff} < 0.15V$, where we match the conditions $qV_{eff} \gg nk_bT$ and $V \gg R_sI$, so that the behaviour of the circuit is driven by the Schottky diode. The surface of the graphene/Schottky junction is $A = 0.0004\ cm^2$, as described in Chapter 3, while the value of the Richardson constant for Ge(001) can be found in literature corresponding to $A^* = 14.4\ A/cm^2K^2$ [15]. The measurements are performed at room temperature, with $T = 293.15K$.

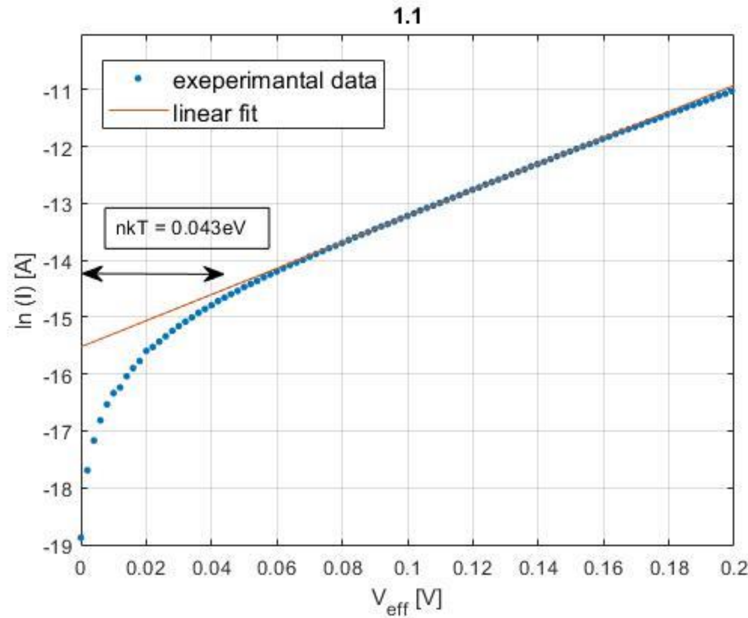

Fig. 4.6 *Linear fit of ln(I) vs V_{eff} for the structure 1.1.*

In Tables 4.1 and 4.2 the experimental values of φ_b and n for all the 46 graphene/Ge structures are reported. The values of φ_b are quite homogeneous between the structures, with an average value of $\varphi_b = 0.534\ eV\ \pm 0.033\ eV$. A theoretical estimation of this value can be calculated using the Schottky-Mott rule (Eq. (1.1.1)). Using $\varphi_M = 4.48\ eV$ for the graphene work function [4,45] and $\chi = 4\ eV$ for the Ge electron affinity, we would expect a Schottky barrier of $\varphi_b = 0.48\ eV$. Deviations from this value could be attributed to the lowering of E_F, as suggested by Ref. [22], due to the natural *p*-doping that occurs during the transfer process of graphene or due the graphene/Au contact [21]. As consequence, we should use a value for the graphene work function larger than the reported one, which is calculated assuming the Fermi level at the Dirac point, resulting in a higher barrier.

Also, the Schottky-Mott rule does not take into account the role of the possible high density of surface states at the interface, and the associated Fermi level pinning.

For the ideality index, the situation is more heterogeneous, as can be seen from Fig. 4.7. In literature, typical values of n for graphene/SC Schottky junction are in the range of 1.2-5.0, with no obvious correlation with the type of substrate [4]. As explained in Chapter 1, n is a phenomenological parameter, included in the equation of the current intensity to consider the deviations from a pure thermionic emission. Good quality junctions have $n \approx 1.0 \div 1.2$ [5], where a unity value for n refers to a pure TE. In this sense, we can consider n as a measure of how defects and other non-thermionic effects mediate the transport, with respect to a pure TE transport.

0,565	0,574	0,562	0,496	0,572	F	0,557
0,563	0,536	0,474	0,563	0,563	0,566	0,554
0,564	0,544	0,498	0,511	0,471	0,465	0,542
0,546	0,560	F	0,508	0,561	0,533	0,493
0,544	0,447	0,521	0,491	0,520	0,537	0,523
F	0,509	0,521	0,537	0,521	0,532	0,521
0,549	0,606	0,604	0,559	0,504	0,503	0,505

Table 4.1 *Experimental values of the Schottky barrier height for the graphene/Ge junctions, obtained from linear interpolation of ln (I) vs* V_{eff}*. Values are reported in eV.*

1,96	1,91	1,84	2,88	1,90	F	2,11
1,91	2,16	3,86	1,99	1,98	1,96	2,02
1,99	2,26	3,39	2,20	4,14	3,54	2,05
2,01	2,01	F	3,53	2,01	2,13	1,78
2,43	1,89	1,8	2,01	1,97	2,23	2,44
F	2,23	1,87	2,05	1,92	1,96	1,94
1,72	3,79	2,06	1,93	2,26	2,03	2,25

Table 4.2 *Experimental values of the ideality index n for the graphene/Ge junctions, obtained from linear interpolation of ln(I) vs* V_{eff}*..*

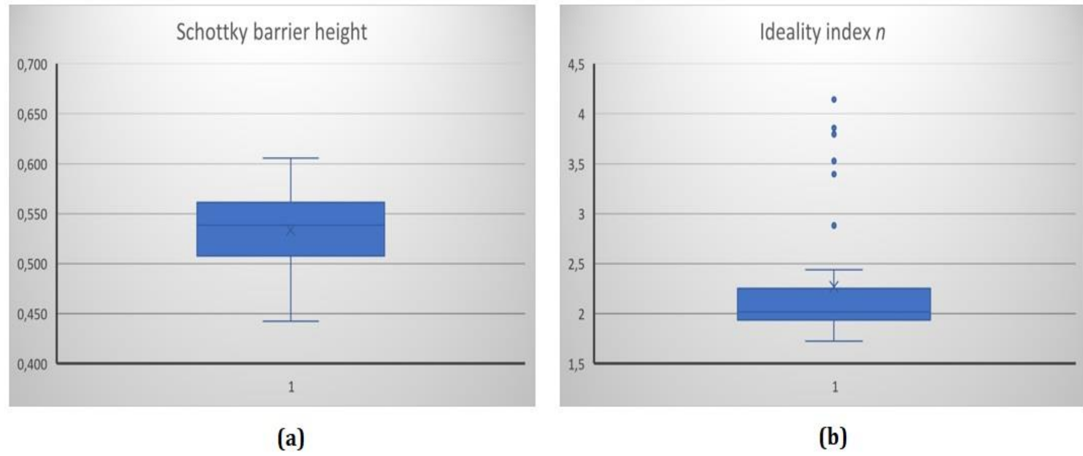

Fig. 4.7 *Boxplot diagrams for the barrier height φ_b and n parameters of the 46 graphene/Ge Schottky structures.*

4.2 Temperature-dependent I-V characterization

To characterize the temperature behaviour of the graphene/Ge Schottky junctions, we measured the *I-V* curve at different temperatures. The sample was connected to the probe as shown in Fig. 4.1 and lied on a heating plate used to set the temperature for the measurement. Fig. 4.8 shows the temperature dependent *I-V* characteristics in semilogarithmic scale. The current is measured over a voltage range between -3V and 0.5V, with a sensitivity of 2 mV in the 19 °C-110 °C temperature range. To calculate the effective voltage dropping on the junction, the series resistance is calculated by linear interpolation of *I* vs *V* for the different temperature, as shown in section 4.1. Using V_{eff}, the actual diode characteristics as a function of temperature is reported in Fig. 4.9, in semilogarithmic scale for the forward bias range. From Fig. 4.8 and 4.9 we notice, for both the bias ranges, a larger intensity current as temperature is increased, since the probability of conduction electrons overcoming the barrier increases. The experimental values of φ_b and n are calculated by the linear fit of the forward bias ln (I) vs V_{eff} at each temperature and are summarized in table 4.3.

	19 °C	30°C	50°C	70°C	80°C	110°C
$\varphi_b[eV]$	0.472	0.484	0.506	0.527	0.549	0.575
n	1.44	1.43	1.38	1.32	1.26	1.17

Table 4.3 *Experimental values for Schottky barrier and n as function of temperature. Values calculated by linear fitting ln(I) vs Veff.*

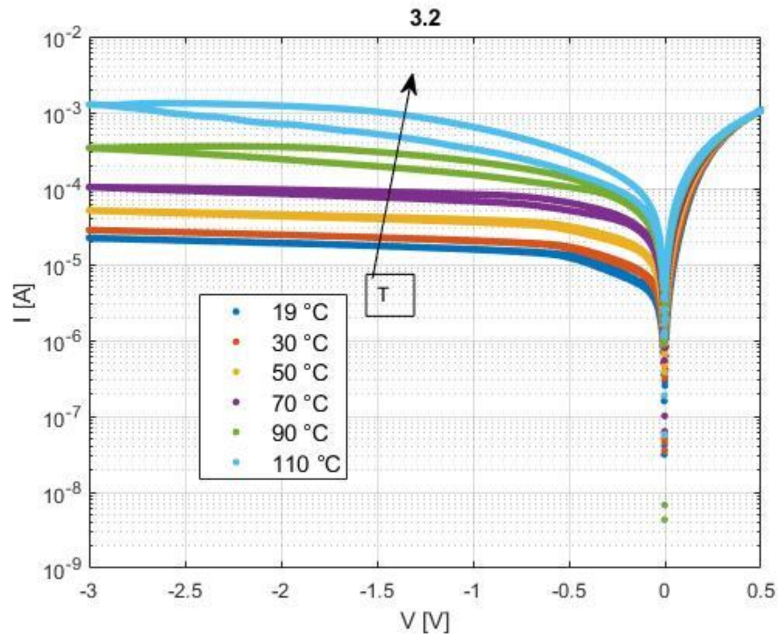

Fig. 4.8 *Semilogarithmic current-voltage (I-V) characteristic of the graphene/Ge SBD in the temperature range 19°C-110°C in the forward and reverse bias range.*

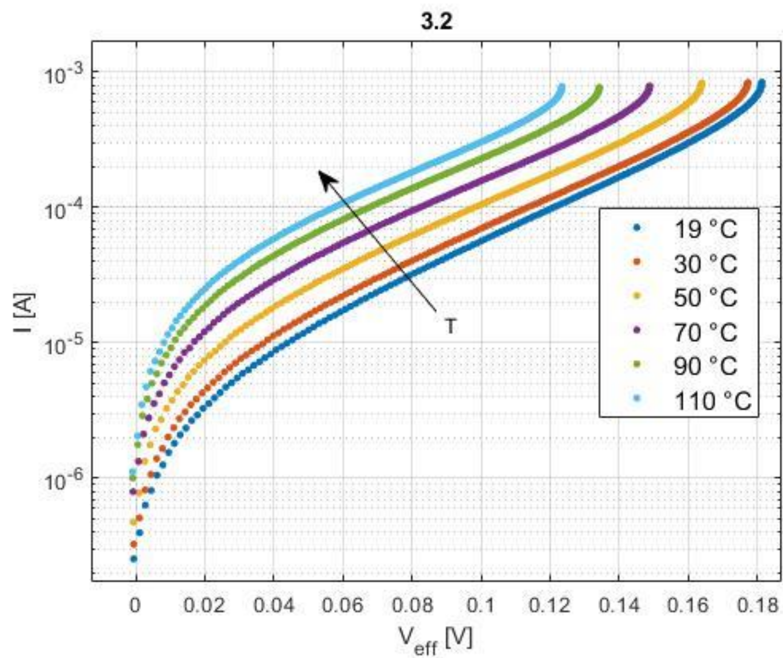

Fig. 4.9 *Semilogarithmic current-effective voltage (I-Veff) characteristic of the graphene/Ge SBD in the temperature range 19 °C-110 °C in the forward bias range.*

It can be observed that both φ_b and n show a correlation with temperature, as they increase with it, indicating a deviation from the pure thermionic emission (TE) behaviour, in which on the contrary they should remain constant. Z. Khurelbaatar [16] suggested that the problem could be related to the spatial inhomogeneity of the Schottky barrier at the graphene/Ge interface. S. Liang et Al. [7] suggested that this feature could be related to the carrier density inhomogeneities in graphene, also known as electron-hole puddles. The electron-hole puddles are the formation of randomly distributed spatial regions in graphene with an excess of electrons and an excess of holes. The origin of this phenomenon is not well understood, although a possible cause can be related to the intrinsic structural wrinkles of graphene and the effect of the substrate interface roughness [24.]. As a consequence of this fluctuations in charge density, the Fermi level is not constant in graphene, giving rise to a not uniform Schottky barrier. At low temperature, the transport is dominated by the low Schottky barrier path, while for higher temperatures, more electrons have enough energy to overcome the higher barriers and therefore the measured effective barrier increases.

The barrier inhomogeneity can be modelled by assuming a gaussian distribution of the barrier, with a mean value $\overline{\varphi_b}$ and a standard deviation σ. Using this model, the temperature dependence for the measured apparent barrier φ_{ap} can be expressed as [17]:

$$\varphi_{ap} = \overline{\varphi_b} - \frac{q\sigma^2}{2kT}. \quad (4.2.1)$$

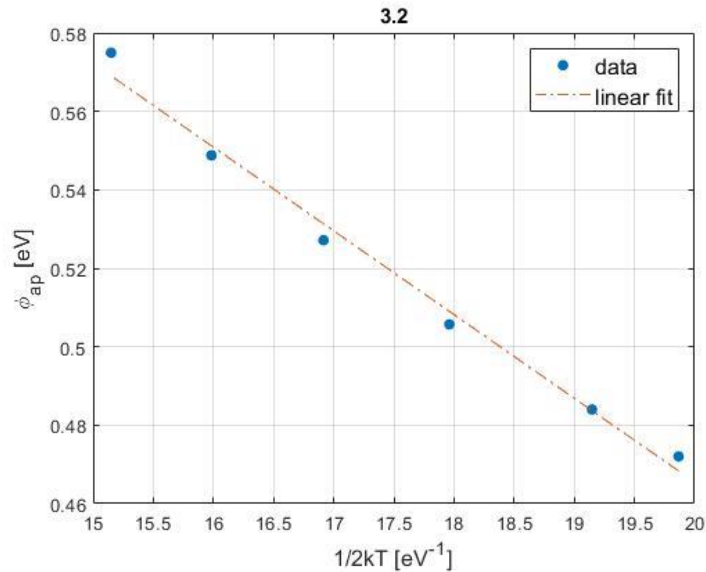

Fig. 4.10 *Plot of φ_{ap} as a function of* $1/2kT$.

If we plot the values of the SBH of table 4.3 as function of $q/2k_bT$ (Fig. 4.10), we should expect a straight line, yielding $\overline{\varphi_b}$ and σ from the intercept and the slope of the linear fit. We obtained, for the structure 3.2, $\varphi_b = 0.89\ eV$ and $\sigma = 0.14\ eV$, which are similar to those obtained in [16] $\varphi_b = 0.87\ eV$ and $\sigma = 0.107\ eV$.

Using the temperature dependent currents, we are also able to calculate the experimental value of the Richardson constant, using the Richardson plot $\ln(I_s)\ vs\ 1/T$. Indeed, in the case of TE, in the limit $qV_{eff} \gg nk_bT$ we have, from Eq. (4.1.2):

$$\ln\left(\frac{I_s}{T^2}\right) = \ln(AA^*) - \frac{q\varphi_b}{k_bT}, \tag{4.2.2}$$

where the slope and the intercept give A^* and φ_b, respectively. The values for I_s as function of temperature are calculated from the linear fit of $\ln(I)\ vs\ V_{eff}$ and the corresponding Richardson plot is shown in Fig. 4.11. The linear behaviour expected from TE is well reproduced, but the experimental value of the Richardson constant is found to be $A^* = 3.58\ 10^{-5}\ A/cm^2K^2$, much lower than the theoretically expected value.

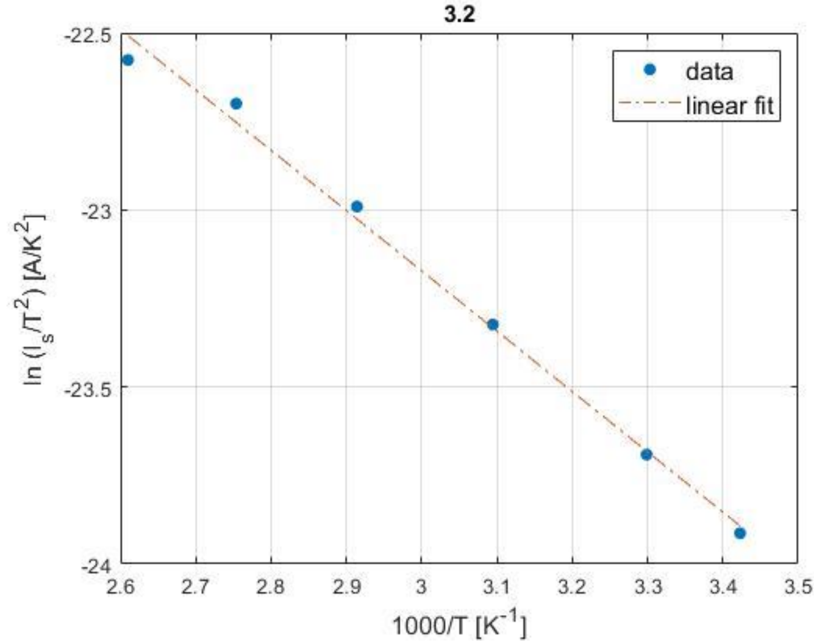

Fig. 4.11 *Richardson plot of ln(Is/T^2) vs 1000/T for the graphene/Ge Schottky structure 3.2.*

Also, this problem can be solved by considering the inhomogeneity of the barrier [16], substituting in Eq. (4.2.2) the expression for φ_{ap} of Eq. (4.2.1) to φ_b. The modified Richardson plot (Fig. 4.12) is now given by the expression:

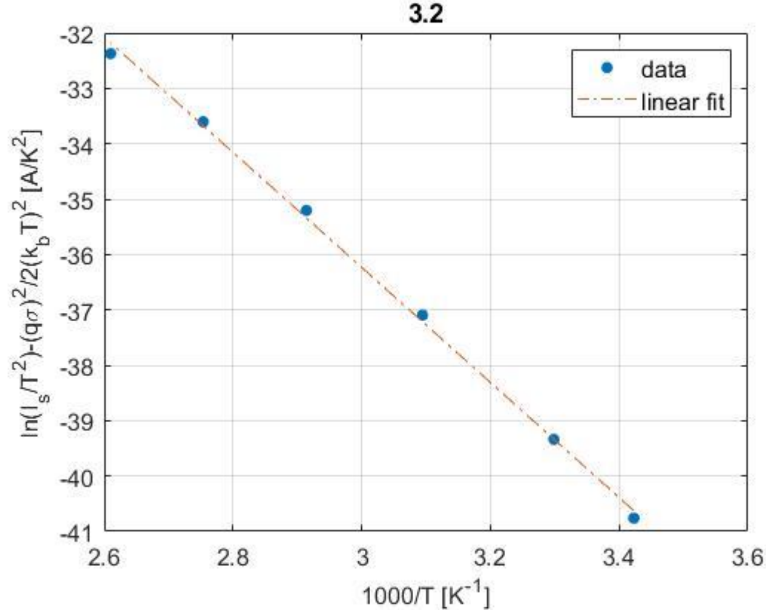

Fig. 4.12 *Modified Richardson plot obtained considering the barrier inhomogeneity effect, for the graphene/Ge structure 3.2.*

$$\ln\left(\frac{I_s}{T^2}\right) - \frac{1}{2}\left(\frac{q\sigma}{k_b T}\right)^2 = \ln(AA^*) - \frac{q\overline{\varphi_b}}{k_b T}. \quad (4.2.3)$$

Using the modified Richardson plot, the Richardson constant is calculated from the intercept of the linear fitting as $A^* = 15.8\, A/cm^2K^2$, in good agreement with the theoretical value of $A^* = 14.4\, A/cm^2K^2$.

Table 4.4 reports the values of $\overline{\varphi_b}$, σ and A^* obtained for the other tested structures.

structure	$\overline{\varphi_b}$ $[eV]$	$\sigma[eV]$	A^* $[A/cm^2K^2]$
1.1	0.92	0.139	14.9
3.2	0.89	0.146	15.8
4.7	0.80	0.125	14.4
7.3	0.96	0.140	14.5

Table 4.4 *Experimental values for* $\overline{\varphi_b}$, σ *and* A^* *obtained for the tested structures. Richardson constant is calculated using the modified Richardson plot.*

4.3 Optical characterization

We optically investigated the formation of the graphene/Ge Schottky junction, measuring the *I-V* characteristic under illumination at different light intensities. As explained in Chapter 1, we should expect that the photocurrent drops to zero approaching the forward bias, while, for higher impinging power, higher saturation is reached for higher reverse bias.

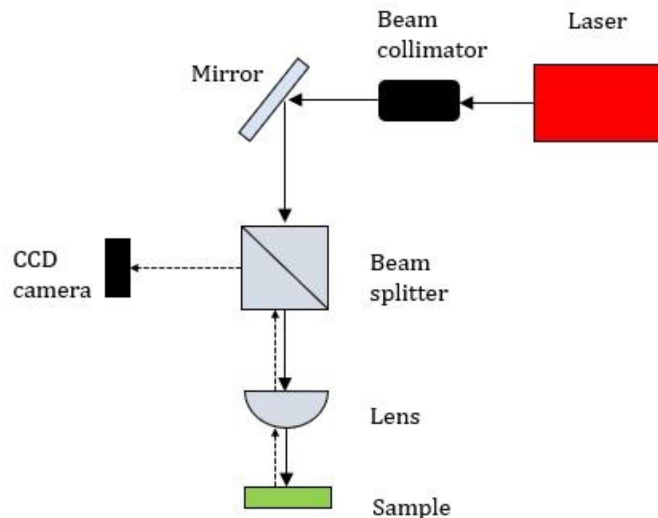

Fig. 4.13 *Optical set-up for the I-V measurement under illumination.*

The optical set-up is shown in Fig. 4.13. A 0.8 eV collimated laser beam is deflected by a mirror and, after passing through a 50:50 beam splitter, is focused on the sample, which is sticked in vertical position on a multiaxial stage. A CCD camera detects half of the light reflected by the sample, so that we are able to see where the beam is illuminating the sample and, moving the multiaxial stage, to focus the beam on the graphene/Ge Schottky junction under study.

The sample is connected as shown in Fig. 4.1 (a) to a Keithley source meter, which applies a bias from -5V to 1V, with a sensitivity of 2 mV. The measurement is performed changing the intensity of the laser and its power is measured using an infrared Ge power-meter The result of the measurement is shown in Fig. 4.14. We can see that the photocurrent drops to zero as the forward bias approaches zero and, for higher impinging power, the photocurrent reaches higher values but for higher reverse bias. This peculiar behaviour of the graphene/SC junctions can be seen a further proof that the graphene/Ge Schottky junction was correctly fabricated.

However, the photocurrent does not reach a steady state saturation value but drops to zero as the bias reaches -5 V, the reason of which is not well understood.

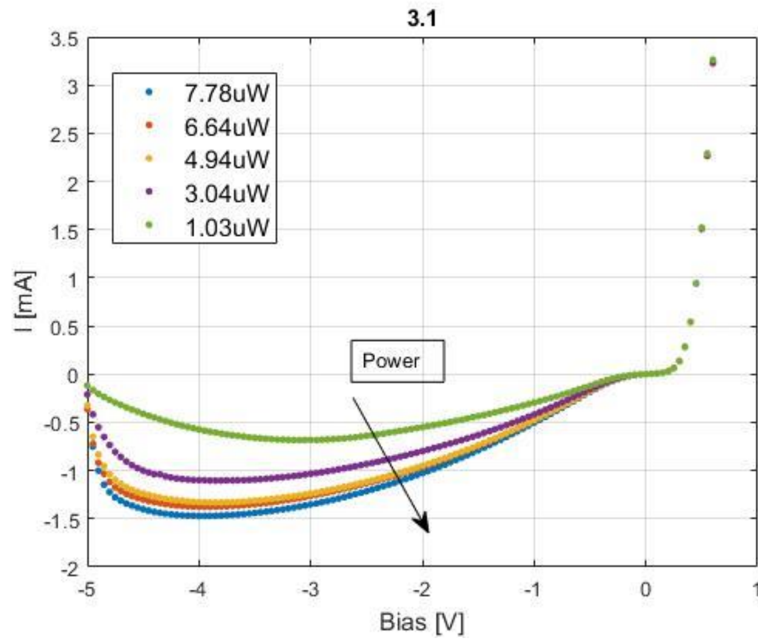

Fig. 4.14 *I-V curve for the graphene/Ge photodiode under illumination at 0.8 eV for different intensities. As expected from a graphene/Ge photodiode, the photocurrent drops to zero at 0 bias.*

Chapter 5
ISHE measurement

In this chapter the diffusion of the optically generated spin current from Ge to graphene is tested by means of the inverse spin-Hall effect (ISHE), and its transport through the graphene layer. The ISHE signal is measured at the edge of the Pt pad. To prove that the measured signal ΔV is actually correlated to ISHE generated by the spin current transported by graphene, we exploited the correlation between the acquired data and the ISHE dependences shown in Section 2.2: we measured the signal spectrum, its dependence from the light polarization and incident power and the dependence upon the incidence angle of the light beam with respect to the sample surface. Finally, we also tested how the signal changes changing the beam spot's position on the graphene/Ge Schottky junction.

The first section of the chapter shows the experimental set-up used for the measurements and describes how the signal is collected, while the second section shows the different analysis on the data. All the measurements have been performed at the SemiSpin Lab of Politecnico di Milano.

5.1 Setup for generation and measurement of spin-to-charge conversion

To inject a spin current in the graphene layer, we need to shine with CPL the graphene/Ge Schottky junction, generating a spin polarized electrons population in the conduction band of the Ge substrate. Such a spin population eventually diffuses form Ge to graphene, then reaching the Pt pad where, through ISHE, the spin current is converted into charge current. Under open-circuit condition, it is generated a voltage drop ΔV_{ISHE} opposed to the electromotive force generating the

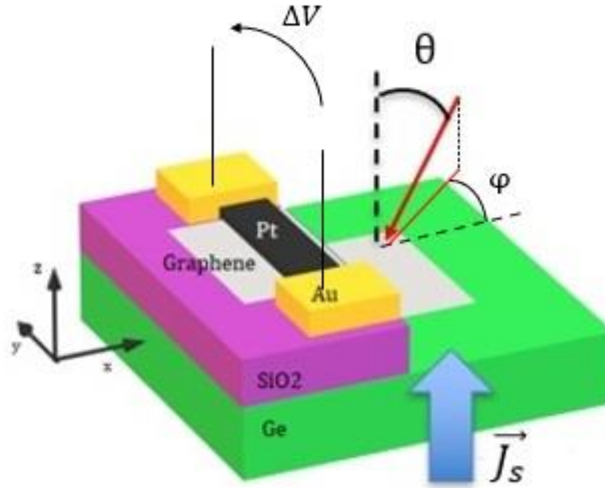

Fig. 5.1 *Sketch of the optical generation and detection of spin currents in graphene.*

charge current, which can be detected measuring the voltage drop across the Pt pad, as explained in Section 2.2. Therefore, measuring this voltage drop, we should be able to see if we succeeded in the generation on spin current in graphene. A sketch illustrating the generation and detection of spin current in graphene is shown in Fig. 5.1. Given the geometry of Fig. 5.1 and given the expression for the ISHE electromotive field:

$$\boldsymbol{E}_{ISHE} \propto \boldsymbol{J}_S \times \boldsymbol{u}_S, \tag{5.1.1}$$

it is clear that, to detect an ISHE signal, we must be able to generate a spin current with an in-plane spin component, a condition which is fulfilled illuminating the sample at grazing incidence, as explained in Chapter 2. The experimental setup is shown in Fig. 5.2. With this setup, we are able to:

- generate a collimated monochromatic light in a NIR-visible range,
- generate a circularly polarized light,
- focus the light on the sample at grazing angle.

We will now discuss each part of the setup and understand its different features.

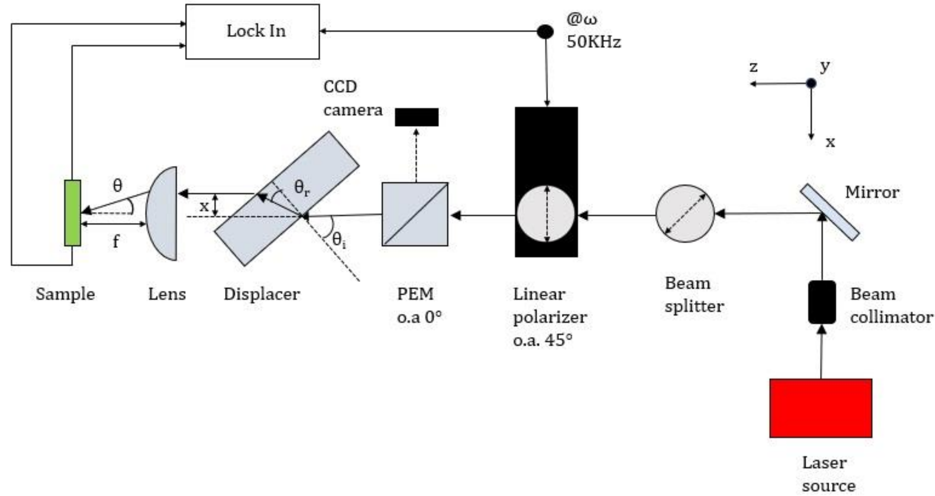

Fig. 5.2 *Experimental setup for the generation of spin current in graphene and measurement of the ISHE signal.*

5.1.1 Laser source

The laser source is made by two sections: a first section, the actual laser source, which produces a white light, and a monochromator section, where the white light is diffracted in its spectral component and the correct wavelength for the measurement is selected. The white light is generated by a *SuperK Extreme NKT Photonics* supercontinuum laser, that emits pulses in the nanosecond range at 78 MHz repetition rate, tuned at the Nd YAG photon energy of 1.16 eV, with a power of 2 W when operating at 100% of power. The pulses enter in a photonic crystal fiber where, through non-linear effects, the power is spread over a 0.5 eV-3.1 eV energy range. To select the correct photon energy for the measurement, the white light enters in a Pellin-Broca prism, which separates the spectral components. The geometry of the Pellin-Broca prism is such that, for a given orientation of the prism, only the light with a given photon energy is deviated by 90° with respect to the direction it enters the prism. Then, a system of mirrors deviates that light beam towards a cylindrical lens, that focuses it into a multimode fiber which brings the light with the desired photon energy into the optical system. The Pellin-Broca prism is placed on a motorized stage, controlled by a *LabView* dedicated program. By rotating the prism around the point *O* (Fig. 5.3 (a)), we are able to select the different photon energies used for the experiments. The power spectrum is measured between 0.8 eV and 2 eV using a Ge based power-meter and a Si based power-meter for NIR and visible range, respectively, and it is shown in Fig.5.3 (b). The peak in the power spectrum corresponds to the fundamental (pump) light beam at 1.16 eV. The total power emitted by the laser source can be also reduced from the

original 2W, when operating at 100% power. This feature is used to change the power of the laser when measuring the ISHE signal at different light intensities.

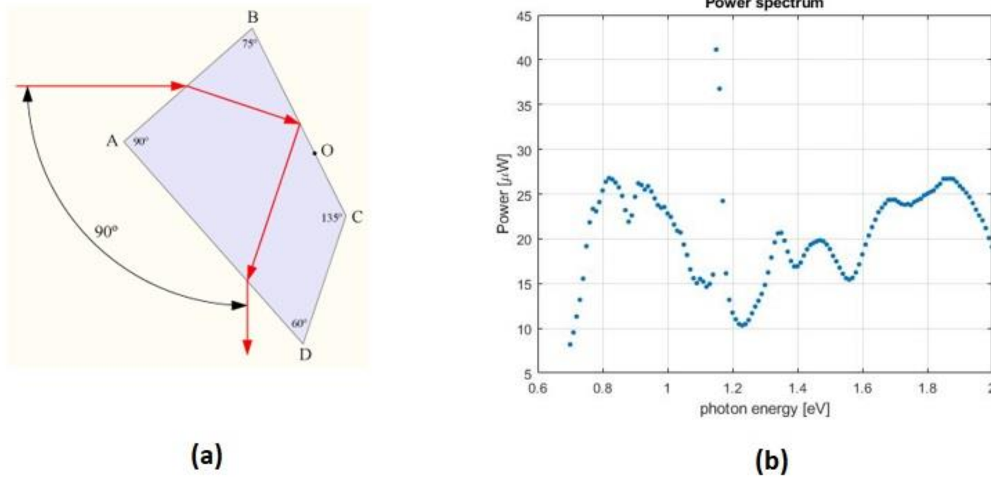

***Fig. 5.3** (**a**) Pellin-Broca prism used to separate the spectral components of the white light beam. By rotating the prism around the point O, we change the spectral component that is deviated by 90°. (**b**) Power spectrum between 0.7eV-2 eV collected at the output of the fiber.*

5.1.2 Generation of modulated CPL

The polarization state of the light that exits from the source depends on the emission power, but it is usually elliptically polarized for low power or not polarized for higher power [47]. The generation of circularly polarized light is obtained combining a linear polarizer (LP) and photoelastic modulator (PEM). To maximize the degree of circular polarization (DCP) the relative angle between the optical axis of the LP and of the PEM has to be of 45°. Moreover, with the PEM we are able to modulate in time the DCP, which allows us to perform a lock-in detection of the ISHE signal, as explained later.

The working principle of the PEM is the photoelastic effect, in which a mechanically stressed material shows birefringence linearly dependent on the applied strain. A PEM consists of a piezoelectric transducer and a transparent resonant bar, usually made of silica. By applying a voltage to the piezoelectric, the latter applies a strain along the optical axis of the silica (x-axis in Fig. 5.2) changing its refractive index. As an electromagnetic wave propagates through the silica, the electric field components projected along the optical axis (x-axis in our case) and along the orthogonal y-axis will experience a different refractive index and will accumulate a phase difference:

$$\Delta\varphi = (n_x - n_y)\frac{2\pi}{\lambda}t, \tag{5.1.2}$$

where t is the thickness of the silica bar and λ is the electromagnetic wavelength. The phase shift is linearly dependent from the applied strain, which is linearly controlled by the voltage applied to the piezoelectric. Therefore, by modulating this voltage at the resonant frequency of the bar (50 kHz in our case), we are able to modulate the phase shift, as [41]:

$$\Delta\varphi = \Delta\varphi_0 \cos(\omega_m t) = \frac{GV_m}{\lambda}\cos(\omega_m t), \tag{5.1.3}$$

where ω_m is the angular frequency of the modulation, V_m is the maximum applied voltage and G is a constant independent from both V_m and λ.

The behaviour of the electric field in the LP-PEM system can be described using the Jones matrixes formalism. In this frame, the electric field's *x-y* components are represented by the Jones vector as:

$$\boldsymbol{E} = \begin{bmatrix} E_{0,x}e^{i\varphi_x} \\ E_{0,y}e^{i\varphi_y} \end{bmatrix}, \tag{5.1.4}$$

where $E_{0,x}$ ($E_{0,y}$) and φ_x (φ_y) are the amplitude and the phase of the *x (y)* component of the electric field. The common phase term $e^{i(kz-\omega t)}$ is omitted in the Jones formalism. The electric field coming out from the LP is expressed, for a generic angle α of the optical axis with respect to the *x*-axis, as:

$$\boldsymbol{E}_{in} = \begin{bmatrix} E_0\cos(\alpha) \\ E_0\sin(\alpha) \end{bmatrix}. \tag{5.1.5}$$

The effect of the PEM can be described by the matrix:

$$\boldsymbol{M} = \begin{bmatrix} 1 & 0 \\ 0 & e^{-i\Delta\varphi} \end{bmatrix}, \tag{5.1.6}$$

where $\Delta\varphi$ is the phase difference, as shown in Eq. (5.1.3). The expression for the electric field of the light out of the PEM is given by the relation:

$$\boldsymbol{E}_{out} = \boldsymbol{M} \cdot \boldsymbol{E}_{in} = \begin{bmatrix} E_0\cos(\alpha) \\ E_0\sin(\alpha)e^{-i\Delta\varphi} \end{bmatrix}. \tag{5.1.7}$$

The expression for the field in Eq. (5.1.7) is expressed in the generic base $\begin{pmatrix} 1 \\ 0 \end{pmatrix}$, $\begin{pmatrix} 0 \\ 1 \end{pmatrix}$, which correspond to a field linearly polarized along the *x* and *y* components. If we want to calculate the DCP of the light, it is more convenient to express Eq. (5.1.7) in the base of right and left circularly polarized light, given by:

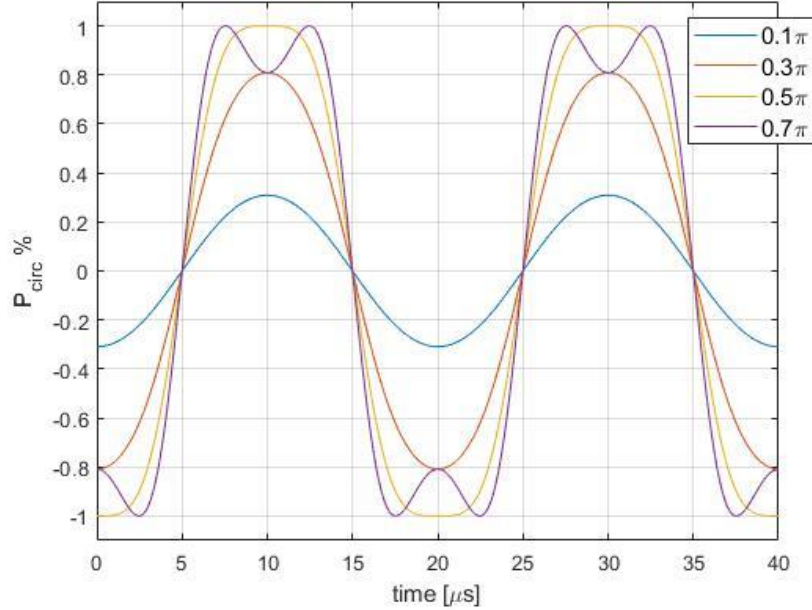

Fig. 5.4 *Degree of circularly polarization as function of time at the output of the PEM section, for different values of Δφ0. The light entering the PEM is linearly polarized with an angle of 45° with respect to the PEM optical axis.*

$$|R\rangle = \frac{1}{\sqrt{2}}\binom{1}{-i}, \quad |L\rangle = \frac{1}{\sqrt{2}}\binom{1}{i}, \tag{5.1.8}$$

and a generic Jones vector projected on this basis can be written as:

$$\boldsymbol{E} = r|R\rangle + l|L\rangle. \tag{5.1.9}$$

Since the light intensity $I \propto \boldsymbol{E}^* \cdot \boldsymbol{E} = |\boldsymbol{E}|^2$, we can see that r^*r and l^*l are proportional to the fraction of right and left circularly polarized photons, respectively. We can than write the DCP as:

$$P_{dcp} = \frac{I_+ - I_-}{I_+ + I_-} = \frac{r^*r - l^*l}{r^*r + l^*l}. \tag{5.1.10}$$

For the electric field that exits from the PEM, the coefficient r and l can be calculated with the cross product $\langle \boldsymbol{E}_{out}|R\rangle$ and $\langle \boldsymbol{E}_{out}|L\rangle$, respectively. Using these coefficients, Eq. (5.1.7) and Eq. (5.1.10) we find that the DCP of the light after the LP-PEM stage is:

$$P_{dcp} = -\sin(\Delta\varphi)\sin(2\alpha). \tag{5.1.11}$$

The expression is maximized for $\alpha = 45°$, which justifies the choice in our set up. Since $\Delta\varphi$ is modulated as shown in Eq. (5.1.3), this modulation is retrieved also in

the DCP. As shown in Fig. 5.4, for a $\Delta\varphi_0 = \pi/2$ we obtain a 50 KHz sinusoidal oscillation between fully RCP and fully LCP states: the PEM is indeed modulating the *x-y* components phase shift between $\pi/2$ and $-\pi/2$. For larger values of $\Delta\varphi_0$, the signal is subjected to overmodulation, while for lower values of $\Delta\varphi_0$ the polarization is still sinusoidally modulated, but with a lower DCP. Since $\Delta\varphi_0$ depends on the wavelength and on V_m (Eq. (5.1.3)), by applying the correct voltage to the PEM we are able to obtain the desired DCP for the selected wavelength. The control of V_m is done by remote, with a dedicated LabView program.

5.1.3 Illumination at grazing incidence

The next step is to focus it on graphene/Ge Schottky junction that we want to study. The sample is mounted on a multiaxial stage and the light beam is focused on it by a *Nikon S-Plan Flour ELWD 60x* objective, which ensures a spot size on the sample of the order of λ. The multiaxial stage allows performing fine tunings of the beam position in in the *x-y* plane and in the *z* plane. The movement in *z* plane is done to obtain a proper focus of the beam, while by moving the stage in the *x-y* plane we can properly select where the beam is focused. To see the position of the beam on the sample and to adjust the focus, we used a CCD camera: the light reflected by the sample pass through a 50:50 beam splitter (BS) which deviates half of the intensity towards the CCD camera, projecting the image of the illuminated sample on a screen.

The illumination of the sample at grazing incidence was done by placing a displacer between the BS and the objective, as shown in Fig. 5.2. When the displacer is rotated in such a way that the beam is orthogonal to its surface, the beam is aligned to the center of the objective and it is focused on the sample at normal incidence. By rotating the displacer, due to the refraction of the beam, the beam is translated by a quantity d from the original direction. As consequence, the beam enters off axis the objective and it is focused on the sample with a polar angle θ with respect to the normal to the sample surface. The relation between the rotation of the displacer θ_i and θ can be found from the Snell law and from simple geometric consideration. We have that, according to Fig. 5.2:

$$\theta = \tan^{-1}(x/f), \quad (5.1.12)$$

where *x* and *f* are the displace of the beam and the distance between the lens and the sample, respectively. *x* is then related to θ_i by:

$$x = d\frac{\sin(\theta_i-\theta_r)}{\cos\ \theta_r} = d\sin(\theta_i)\left(1-\frac{\cos\theta_i}{\sqrt{n_d^2-sin^2\ \theta_i}}\right) \quad (5.1.13)$$

where d and n are the thickness and the refractive index of the displacer, respectively. θ_i is related to θ_r by the Snell law $\sin(\theta_i) = n_d \sin(\theta_r)$, with the refractive index of air assumed to be 1.

5.1.4 Lock-in measurement of ΔV

To retrieve the ISHE signal generated by the spin-to-charge conversion, we measure under open-circuit condition the voltage drop across the Pt pad. Since the DCP is modulated at 50 kHz, and the ISHE signal is linearly dependent on the DCP, as seen in Section 2.2, the latter will also be modulated at the same frequency. We can now retrieve the ISHE signal with a lock-in detection, used to extract a signal with a known carrier modulation from a noisy environment. The lock-in amplifier combines a mixer and a low pass filter (LPF) and takes advantages of the Fourier analysis of periodic functions. A periodic function with frequency f_s and phase Ω can be written as a linear combination of sinusoidal and cosinusoidal functions:

$$V_s(t) = \frac{a_0}{2} + \sum_n a_n\cos(2\pi n f_s t + \Omega) + \sum_n b_n\sin(2\pi n f_s t + \Omega). \quad (5.1.14)$$

By multiplying the signal V_s for a reference cosine signal at the frequency f_s, only the first harmonic term passes through the LPF, while all the other terms are averaged out. We obtain the so called in-phase component, $X = R\ cos(\Omega)$. By multiplying the signal for a sine reference signal, always resonant with the first harmonic, we obtain this time the quadrature component $Y = R\sin(\Omega)$. Once the lock-in has measure the in-phase and the quadrature component, the amplitude and the phase of the signal are calculated as:

$$R = \sqrt{X^2+Y^2} \quad (5.1.15\ a)$$

$$\Omega = \tan^{-1}(\frac{Y}{X}). \quad (5.1.15\ b)$$

In our case, we have that, given the modulation imposed by the PEM:

$$\Delta V(t) \propto |V_{ISHE}|\sin(\Delta\varphi_0\cos(\omega_m t+\Omega)) \approx |V_{ISHE}|[-2J_1(\Delta\varphi_0)\cos(\omega_m t+\Omega) + 2J_3\cos(\Delta\varphi_0)\cos(3(\omega_m t+\Omega)) \ldots \quad (5.1.16)$$

where J_i is the Bessel function of the first kind of other i and $\omega_m = 2\pi * 50kHz$. Using a reference signal at 50 kHz, the lock-in is sensitive to the first harmonic and we can calculate the ISHE amplitude and phase using Eq. (5.1.15).

5.2 Characterization of the ISHE signal

In the previous section we have seen how, using a modulated DCP and a lock-in amplifier, we are able, in principle, to filter the ISHE signal out of the ΔV signal measured across the Pt pad. We need to test this signal to be sure of its ISHE origin. In Section 2.2 we have seen the main dependences of the ISHE signal, which can be written as:

$$\Delta V_{ISHE} \propto P_{s,Ge}(h\upsilon)P_{dcp}I_{in}cos\varphi, \tag{5.2.1}$$

where $P_{s,Ge}(h\upsilon)$ is the photon-energy dependent spin polarization of the photoexcited electrons in the CB of Ge, P_{dcp} and I_{in} are the degree of circular polarization and the light intensity of the incoming beam, and φ is the azimuthal angle, according to the geometry of Fig. 5.1. In the next sections, we will show the characterization of the ISHE signal according to these parameters and their results.

5.2.1 Photon energy dependence the of ISHE signal

The data are collected with $P_{dcp} = 100\%$ (full circular polarization) and with the displacer rotated by $\theta_i = 60°$ while the azimuthal angle is $\varphi = 0$. To better filter the signal, we the measurement is performed with a double modulation. A chopper placed before the LP modulates the intensity of the signal at 21 Hz, while the LP-PEM system modulate the DCP at 50 kHz, as explained before. The signal measured across the Pt pad is recorded by a first lock-in amplifier which performs a first demodulation at 50 kHz, of which the output is measured by a second lock-in, which demodulates it with a reference signal at 21 Hz and gives the in phase and quadrature phase components. The signal is measured varying the photon energy $h\upsilon$ from 0.7 eV to 2 eV, with a step of 5 meV, with the beam focused on the middle of the squared graphene/Ge Schottky junction. For each photon energy, we acquired three measures to reduce the noise.

To properly compare the ISHE signal at different photon energy, we need to normalize it to the photon flux. Indeed, the ISHE for a given photon energy does not depend just on the spin polarization generated in Ge at that energy, but also on photon flux at that energy, which influences how many carriers are generated. Since the photon flux emitted by the laser is not uniform in the whole spectrum, we need to normalize the IHSE signal to the photon flux, as:

$$\Delta V_{ISHE}^{norm}(h\upsilon) = \frac{\Delta V_{ISHE}(h\upsilon)}{\Phi(h\upsilon)_{Ge}}, \tag{5.2.2 a}$$

$$\Phi(h\upsilon)_{Ge} = \frac{W(h\upsilon)T(h\upsilon)(1-\alpha_{gr})}{h\upsilon\, \pi(^{\lambda}/_{2})^2} \quad (5.2.2\text{ b})$$

where $\Phi(h\upsilon)_{Ge}$ is the photon flux impinging on Ge. The photon flux is calculated assuming that the spot size on Ge is a circle with radius λ, wavelength of the incoming beam. The power spectrum emitted $W(h\upsilon)$ by the source is measured using Ge-based power meter for the range 0.7 eV – 1.15 eV and Si based power meter in the range 1.5 eV – 2 eV, placed before the objective. The power that is transmitted to Ge is than calculated by multiplying $W(h\upsilon)$ for the transmittance $T(h\upsilon)$ of the objective and for the transmittance of graphene $(1-\alpha_{gr})$, where the absorption coefficient of graphene α_{gr} is assumed to be constant is the spectral range 0.7 eV – 2 eV.

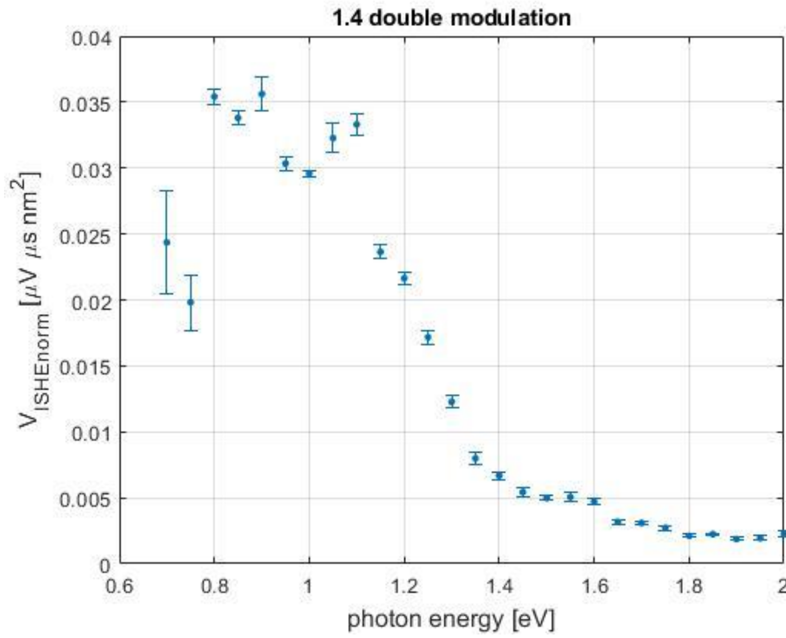

Fig. 5.5 *Spectral dynamics of the normalized ISHE signal for the structure 1.4, measured with a double modulation technique.*

The energy dependence of the ISHE signal, normalized to the incident photon flux, is shown in Fig. 5.5. We can observe that it resembles the electron spin polarization spectrum $P_{s,Ge}(h\upsilon)$, as expected from Eq. (5.2.1). The sharp decrease of the electron spin polarization expected for $h\upsilon = E_g + \Delta_0$ due to the excitation of electron from the SO band, is found in the measurement at about 1.2 eV, so 0.1 eV higher than the theoretically expected value. This effect can be related to the different depth at which electrons from the HH and the SO bands are promoted to the CB band, as suggested by F. Bottegoni and Al. in Ref. [10]. Indeed, at a first approximation, the

absorption coefficient for direct gap transitions is proportional to $m_r^{(3/2)}\sqrt{h\upsilon - E_t}$, being m_r the valence/conduction band reduced mass at Γ and E_t the threshold energy of the transition. For the transition from the HH and SO bands to the CB at Γ, we have that $m_r = 0.037, E_t = 0.8\, eV$ and $m_r = 0.028, E_t = 1.1\, eV$, respectively. When we illuminate with, for instance, RCP photons with 1.1 eV energy, the absorption coefficient for the excitation of spin up electrons in the CB from the SO band is roughly ten times smaller than the one for the excitation of spin down electrons in the CB from the HH band. Therefore, for a photon energy of 1.1 eV, the spin down electrons excited from the SO band are generated further away from the graphene/Ge interface. As they will have to diffuse in Ge before entering in the graphene layer, they will be more affected by spin relaxation in Ge, giving a minor contribution to spin polarization of the current injected in graphene. It should be notice that, in the optical orientation process, we also generate spin polarized holes. However, since the spin lifetime for holes in Ge is few hundreds of femtoseconds, much shorter than the one for electrons (~ ns) [12], they will give a negligeable contribution to the ISHE signal.

5.2.2 ISHE as a function of the degree of circular polarization and light power

We expected the ISHE signal to be linearly dependent on the DCP and on the power of the incoming light beam. Indeed, the ISHE signal is proportional to the spin current density defined as $\boldsymbol{J}_s = qnP_s\boldsymbol{v}$, where n and P_s are the density of photoexcited electrons and their spin polarization. For a higher DCP, the light transports a higher angular momentum which can be transferred to the excited electrons, resulting in a higher P_s. On the other hand, a higher power determines a higher number of excited electrons.

The measurement of ISHE as a function of DCP are performed with the displacer rotate by $\theta_i = 40°$, while the azimuthal angle is $\varphi = 0$. The photon energy is fixed at 0.8 eV, corresponding to an incident power absorbed by Ge of $W_{Ge} = 7.78\mu W$, and the beam is focused on the middle of the graphene/Ge Schottky junction. The DCP is varied between 10% and 100%. The results are shown in Fig.5.6 (a). The measured values are normalized to the highest signal for $P_{dcp} = 100\%$. We can observe a linear dependence between the ISHE signal and the DCP, as also suggested by the linear fit. We can also observe that the linear fit intercepts the ISHE signal at 0V for $P_{dcp} = 0$, i.e. that we expect no ISHE signal for a linearly

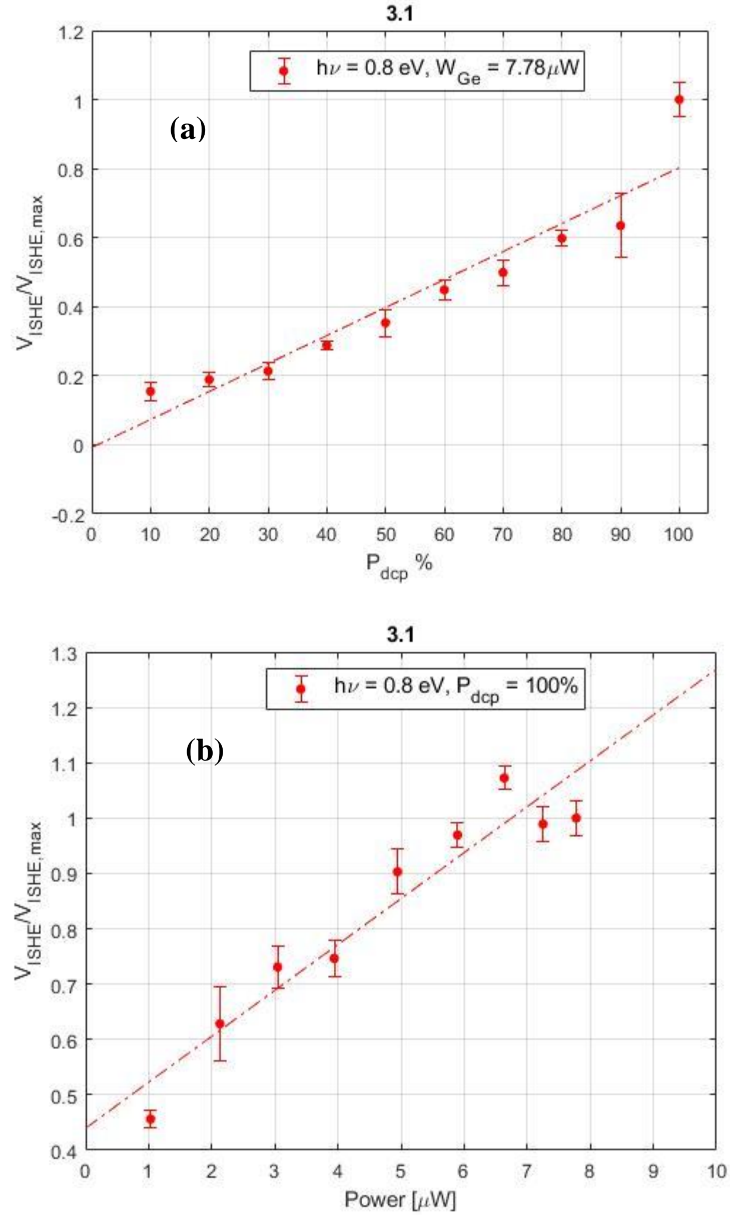

Fig. 5.6 *ISHE signal as a function of* ***(a)*** *the degree of circular polarization and* ***(b)*** *light beam power, for fixed photon energy of 0.8 eV.*

polarized light, coherently with the fact that with linearly polarized light, which carries no net angular momentum, we do not generate a net electron spin polarization.

The measurement of the ISHE signal as a function of the incident power on the sample are performed in the same condition as before for θ_i and φ. The degree of

circular polarization is fixed at $P_{dcp} = 100\%$. Fig. 5.6 (b) shows the result for a photon energy $h\upsilon = 0.8\ eV$, changing the operating power of laser source from 20% to 100%. Again, the signals are normalized to the signal taken at maximum power.

5.2.3 Measurement of the signal phase

An important test to verify the ISHE nature of the signal is the measurement of the signal phase Ω (Eq. (5.1.15 b)) varying the polar angle. Indeed, we can see from Eq. (5.1.1) that the sign of the ISHE signal depends on the direction of the in-plane component of the spin polarization. When we change the polar angle from values $< 0°$ to values $> 0°$, we rotate by π the projection of the wave-vector in the plane of the sample, and so does the in-plane component of the spin polarization. As a consequence, the ISHE signal changes sign, which should be detected by measuring a π shift in the signal phase when the polar angle crosses 0°.

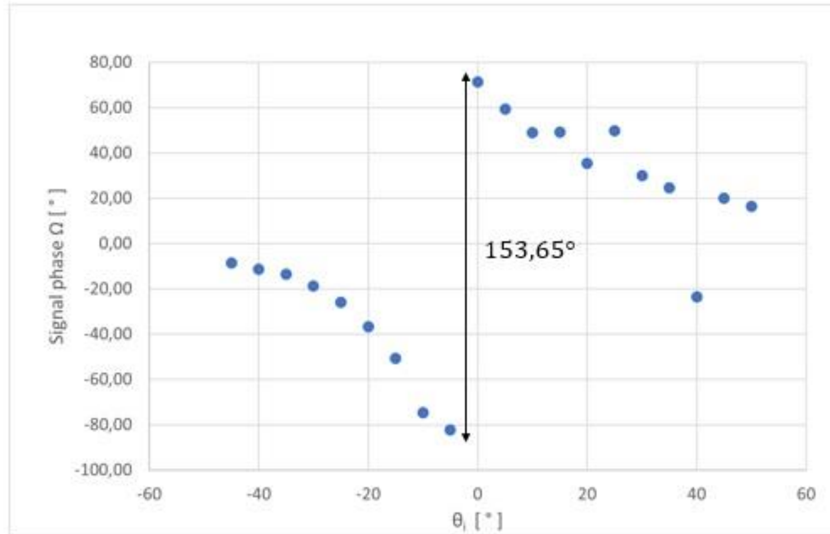

Fig. 5.7 *Phase of the ISHE signal vs the rotation of the displacer.*

We measure the X and Y components of the signal with the lock-in. The photon energy is set to $h\upsilon = 0.8\ eV$, and the incident power on Ge is $W_{Ge} = 7.48\ eV$. The light is fully circularly polarized, $P_{dcp} = 100\%$ and the beam is focused on the middle of the graphene/Ge Schottky junction. We changed the polar angle rotating the displacer between $\theta_i = -45°$ and $\theta_i = 50°$, with a step of 5°. The signal phase is shown in Fig. 5.7 as a function of the rotation angle of the displacer θ_i. We measure a phase shift of 153.65° at $\theta_i = 0°$, which is sufficiently indicative of a sign variation in the ISHE signal.

5.2.4 Analysis of ISHE signal for different positions of the spot

Once we tested the ISHE nature of the measured signal, we tested the ISHE signal illuminating at different distances from the Pt detector. We would expect that, as the spin density is generated further away from the Pt pad, the electrons diffuse along a larger distance than the electrons generated near the Pt pad, before reaching the ISHE detector. The spin relaxation in graphene will reduce the net spin density giving rise to a lower ISHE signal. In a simple 1D model, the relation between the ISHE signal and the spin diffusion length in graphene $l_{sf,gr}$ can be written as [13]:

$$\Delta V_{ISHE} = Ae^{-x/l_{sf,gr}}, \tag{5.2.3}$$

where $x = 0$ corresponds to the position of the detector.

Fig. 5.8 shows the values for the normalized ISHE signal for a photon energy $h\upsilon = 0.8\ eV$, as function of the distance between the centre of the spot and the Pt pad, d_{sPt}. The light is fully circularly polarized, and the power on Ge is $W_{Ge} = 7.48\ \mu W$. To correctly calculate $d_{\text{s-Pt}}$, we calibrated the movement of the multiaxial stage, using as reference the edges of the graphene/Ge Schottky junction. Knowing that the width of the graphene/Ge area is 200μm and that the distance between the Pt and the graphene/Ge Schottky junction is 10 μm for the structure 3.1, we are able to properly set $d_{\text{s-Pt}}$. We scanned over all the width of the graphene region, with a step of 20 μm. The plot of Fig. 5.8 (a) shows that we were not able to find any correlation between the ISHE signal and position of the spot. However, it should be noticed that the set-up used for the experiment is not the best solution to properly address the distance between the generation and detection point. Indeed, when we shine at grazing incidence, the light forms an oblate and broadened spot on the sample, with the consequence that we are not really able to associate to $d_{\text{s-Pt}}$ the actual distance from the Pt pad and the region where the spin density is generated. The low values measured near the Pt pad can be justified considering that, when we illuminate in that point, we have a lower fraction of light shining the graphene/Ge Schottky junction.

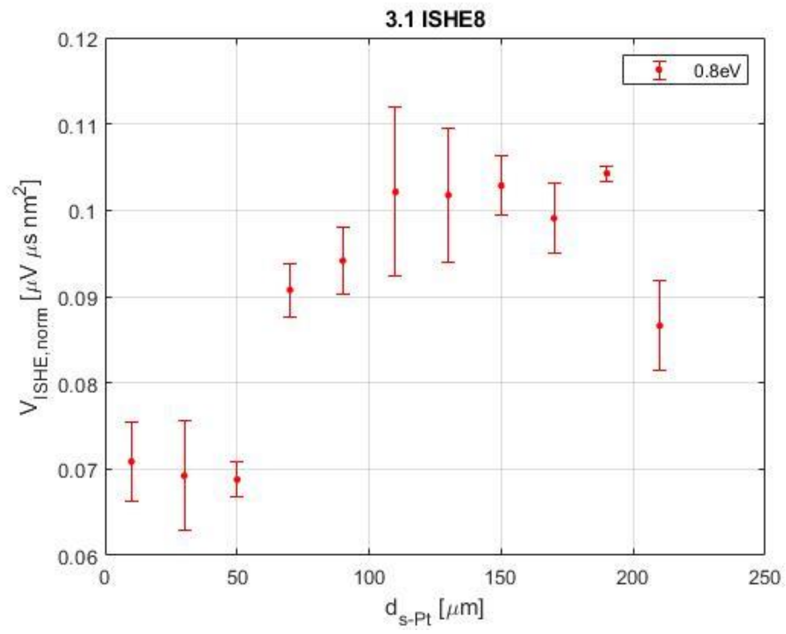

Fig. 5.8 *Normalized ISHE signal for photon energy of 0.8eV as function of the distance between the centre of the spot and the Pt detector.*

Conclusion

At the end of this work, we have been able to prove that graphene/Ge Schottky junctions offer a possible solution for the optical generation of a spin current in a graphene layer. Indeed, the characterizations performed on the signal measured illuminating the structure with circularly polarized light have clearly shown its ISHE origin. Given the design of the structure, the spin current generating the ISHE signal in Pt can only be brought by the graphene layer. This feature also opens the possibility of using graphene as a spin channel transport in devices using ISHE to convert the light polarization information into an electric signal [9].

However, we have not been able to find any correlation between the measured ISHE signal and the spin diffusion length in graphene. The main limitation of the structures used in this work to the study of the spin diffusion length in graphene, is that they need an illumination at grazing incidence to generate an ISHE signal. When we try to focus on the sample an inclined beam, it results in an oblate broadened spot on the sample, with the consequence that we are not able to clearly define the region where we are generating the spin polarized electrons population. A possible solution to generate a in plane spin component illuminating at normal incidence is to pattern the graphene/Ge surface with some thin Pt scatterers. The physics underneath this technique has been analysed by F. Bottegoni in Ref. [12] for a Pt/Ge structure. An in-plane spin component is generated shining with circularly polarized light the edges of the Pt scatterers, generating opposite in-plane spin polarization at opposite edges of the Pt pad. In this way, the normal incidence of the light beam ensures a precise knowledge on where the electron spin population is generated and, scanning over the scatterers, it is possible to generate a spatially sinusoidally modulated signal, with an exponential decay, given by the spin diffusion length. This technique has been used, for example, to calculate the spin diffusion length in Ge by C. Zucchetti et Al. [13].

Bibliography

[1] Wei Han, R.K Kawakami, M. Gmitra, J. Fabian, *Graphene spintronics*, NATURE NANOTECHNOLOGY, Vol 9, October 2014.

[2] N. Tombros, C. Josza, M. Popinciuc, H. T. Jonkman, B.J van Wees, *Electronic spin transport and spin precession in single graphene layers at room temperature,* Nature, Vol 448|2 August 2007.

[3] Y.Liu, C. Zheng, J. Zhong, J. Ding, Z. M. Wang, Z. Liu, *Spintronics in two-dimensional materials*, Nano-Micro Letter, (2020) 12:93.

[4] A. Di Bartolomeo. *Graphene Schottky diodes: An experimental review of the rectifying graphene/semiconductor heterojunction*. Physics Reports, 606:1–58, 2016.

[5] D. K. Schroder. *Semiconductor Material and device characterization,* Third edition, Wiley publications.

[6] C.Xie, Y. Wang, Z. Zhang, D. Wang, L. Luo, *Graphene/Semiconductor hybrid heterostructures for optoelectronic device applications*, Nano Today 19 (2018) 41–83.

[7] S.J. Liang, W.Hu, A. Di Bartolomeo, S. Adam, L.K. Ang, *A modified Schottky model for graphene-semiconductor(3D/2D) contact: a combined theoretical and experimental study.*

[8] S.J. Liang, L.K. Ang. *Electron thermionic emission from graphene and thermionic energy converter,* Physical Review Applied 3(1), 21 Jan 2015.

[9] K. Ando, M. Morikawa, T. Trypiniotis, Y. Fujikawa, C. H. W. Barnes and E. Saitoh,*Photoinduced inverse spin-Hall effect: Conversion of light-polarization information into electric voltage,* APPLIED PHYSICS LETTERS **96**, 082502 (2010).

[10] F.Bottegoni, A. Ferrari, S. Checchi, M. Finazzi, F. Ciccacci and G. Isella, *Photoinduced inverse spin-Hall effect in Pt/Ge(001) at room temperature*, APPLIED PHYSICS LETTERS **102**, 152411 (2013).

[11] C.Zucchetti, M. Bollani, G.Isella, M. Zani, M. Finazzi and F. Bottegoni, *Doping dependence on the electron spin diffusion length in germanium,* APL Mater. **7**, 101122 (2019).

[12] F.Bottegoni, M. Celebrano, M. Bollani, P. Biagioni, G. Isella, F. Ciccacci and M. Finazzi, *Spin voltage generation through optical excitation of complementary spin populations,* Nature Materials, **13**, 790-795(2014).

[13] C.Zucchetti, F. Bottegoni, F. Ciccacci, G. Isella, L. Ghirardini, M. Celebrano, F. Rortais, A. Ferrari, A. Marty, M. Finazzi and M. Jamet, *Imaging spin diffusion in germanium at room temperature,* PHYSICAL REVIEW B **96**, 014403 (2017).

[14] J.E. Hirsch. *Spin Hall Effect*, PHYSICAL REVIEW LETTERS, Volume 83, Number 9, 30 AUGUST 1999.

[15] C.R: Crowell, *Richardson constant and tunnelling effective mass for thermionic and thermionic-field emission in Schottky barrier diodes,* Solid-State Electronics Pergamon Press 1969. Vol. 12, pp. 55-59.

[16] Z.Khurelbaatar, M.S. Kang, K.H. Shim, Y.J. Yun, J. Lee, H. Hong, S.Y. Chang, S.N. Lee and C.J. Choi, *Temperature dependent current-voltage characteristics of Au/n-type Ge Schottky barrier diodes with graphene interlayer,* Journal of Alloys and Compounds 650 (2015) 658-663.

[17] S. Chand and J. Kumar, *Effects of barrier height distribution on the behavior of a Schottky diode*, *1997 American Institute of Physics.* [S0021-8979(97)01422-9].

[18] M. Dyakonov, *Spin-Hall effect.*

[19] M. Dyakonov, *Spin Physics in Semiconductors,* Springer, 2008.

[20] J. Fabian, A. Matos-Abiague, C. Ertler, P. Stano and I. Zutic ,*Semiconductors spintronics*, Springer, 2007.

[21] G. Giovannetti, P.A. Khomyakov, G. Brocks, V.M. Karpan, J. Van den Brink and P.J. Kelly, *Doping graphene with metal contact,* PRL **101,** 026803 (2008).

[22] S. Tongay, M. Lematire, X. Miao, B. Gila, B.R Appleton and A. F. Hebard, *Rectification at Graphene-Semiconductor Interfaces: Zero-Gap Semiconductor Based Diodes,* PHYSICAL REVIEW X 2, 011002 (2012).

[23] X. An, F, Liu, Y. J. Jung and S. Kar, *Tuneable graphene silicon heterojunctions for ultrasensitive photodetection,* Nano Lett. 2013, 13, 909−916

[24] S. Das Sarma, S. Adam, E.H. Hwang and E. Rossi, *Electronic transport in two-dimensional graphene,* REVIEWS OF MODERN PHYSICS, VOLUME 83, APRIL–JUNE 2011.

[25] F. Meier, *Optical Orientation,* Elsevier Science Publishers, 1984, Chapter 2.

[26] J. Rioux and J. E. Sipe, *Optical injection and control in germanium: Thirty-band k·p theory*, PHYSICAL REVIEW B **81**, 155215 _2010.

[27] P.R. Wallace, *The Band theory of graphite,* PHYSICAL REVIEW VOLUME 71, NUMBER 9 MAY 1, 1947.

[28] T. Ando, *The electronic properties of graphene and carbon nanotubes*, *NPG Asia Mater.* **1**(1) 17–21 (2009).

[29] Pezzoli, F. Bottegoni, D. Trivedi, F. Ciccacci, A. Giorgioni, P. Li, S. Cecchi, E. Grilli, Y. Song, M. Guzzi, H. Dery and G. Isella, *Optical spin injection and spin lifetime in Ge heterostructures,* PHYSICAL REVIEW LETTERS **108**, 156603, 13 Apr. 2012.

[30] Y. Yu, M. Cardona, *Fundamental of semiconductors*, Springer, 2010.

[31] M. Dyakonov, *Possibility of orienting electron spins with current,* Journal of Experimental and Theoretical Physics Letters, Vol. 13 p. 467, June 1971.

[32] N. Ashcroft, D. Mervin, *Solid State Physics,* Harcourt College Publishers, 1976.

[33] M. S. Dresselhaus, *Solid state properties, part II: optical properties of solids,* Springer 2018.

[34] C. Zucchetti, *Spin-charge interconversion in Ge-based structures,* Ph.D Dissertation in Physics, Politecnico di Milano, 2019.

[35] C. Zucchetti, *Studio di correnti di spin generate otticamente in giunzioni Pt/Ge mediante effetto spin-Hall inverso,* Tesi di Laurea Magistrale, Politecnico di Milano, 2015.

[36] Y. Shiraki, N.Urami, *Si-Ge Nanostructures – Production, properties and applications in electronics,* Woodhead Publishing, 2011.

[37] G. Isella, *Semiconductor Nanostructures,* Notes on the course of "Semiconductor Nanostructures", Politecnico di Milano, 2019.

[38] H. Jansen, *A survey on the RIE of silicon in microtechnology,* J. Micromech. Microeng. **6** (1996) 14–28.

[39] M. Wojtaszek, N.Tombros, A. Caretta, P. H. M. van Lossdrecht and B. J van Wees, *A road to hydrogenating graphene by a reactive ion etching plasma,* Journal of Applied Physics **110**, 063715 (2011).

[40] R.R. Nair, P. Blake, A. N. Grigorenko, K. S. Novoselov, T. J. Booth, T. Stauber, N. M. R Peres, A. K. Geim, *Fine structure constant defines visual transparency of graphene,* 6 JUNE 2008 VOL 320 SCIENCE.

[41] K. W. Hipps and G.A. Crosby, *Applications of the photoelastic modulator to polarization spectroscopy,* The Journal of Physical Chemistry, Vol. 83 Number 5, March 8, 1979

.